Hu *et al. Biochar* (2026) 8:91
https://doi.org/10.1007/s42773-026-00612-0

Biochar

ORIGINAL RESEARCH Open Access

In-depth into the mechanism of aromatic production from catalytic pyrolysis of wet-torrefied microalgae with HZSM-5 coated biochar

Jinye Hu[1], Yunpu Wang[2], Haiwei Jiang[3], Jiabo Wu[1], Ting Luo[1], Qi Wang[1], Yuhang Hu[1], Kaisong Hu[1], Wenguang Zhou[1] and Liangliang Fan[1*]

Abstract

Bio-oil from pyrolysis of microalgal biomass tends to exhibit high oxygen and nitrogen content, which is challenging for the commercial application of algae-based fuels. This study started with wet torrefaction of *Chlorella* to improve its fuel properties, and then Zeolite Socony Mobile-5 (HZSM-5) was used to synthesize HZSM-5 coated biochar (HZSM-5@biochar) catalyst for catalytic pyrolysis. During the process, up to 96.06% of aromatics with benzene, toluene and xylene (BTX) selectivity of 83.24% and a yield of 94.64 mg g^{-1} was obtained under specific conditions (wet torrefaction at 200 °C, pyrolysis at 500 °C, catalyst-to-feedstock ratio of 20:1). Meanwhile, the content of oxygenates and nitrogenates was reduced from 82.14% under non-catalytic condition to 3.26%. The catalytic conversion pathway was hypothesized by catalytic experiments with model compounds. The transformation process of oxygen- and nitrogen-containing functional groups was probed by XPS and in situ DRIFTS to help elucidate the deoxygenation and denitrogenation mechanism during the catalytic pyrolysis of *Chlorella*. Besides, the excellent stability of HZSM-5@biochar was demonstrated by six-cycle experiments. The composite catalyst also showed lower yield of coke (0.33%) with less aromaticity after a single use compared to HZSM-5, whose coke yield was 1.87%. Scanning electron microscopy analysis revealed that compared to HZSM-5@biochar, the used HZSM-5 formed more amorphous components suspected to be coke.

Highlights

- Wet torrefaction enables preliminary deoxygenation and denitrogenation of microalgae.
- HZSM-5@biochar exhibits outstanding catalytic performance (96% aromatic selectivity) and stability.
- Biochar in the composite catalyst preferentially breaks unstable bonds, thereby suppressing catalyst coking and deactivation.

Keywords HZSM-5@biochar, Aromatic hydrocarbons, Deoxygenation and denitrogenation, Biomass catalytic pyrolysis, Catalyst stability

*Correspondence:
Liangliang Fan
fanliangliang@ncu.edu.cn
Full list of author information is available at the end of the article

Springer

Graphical Abstract

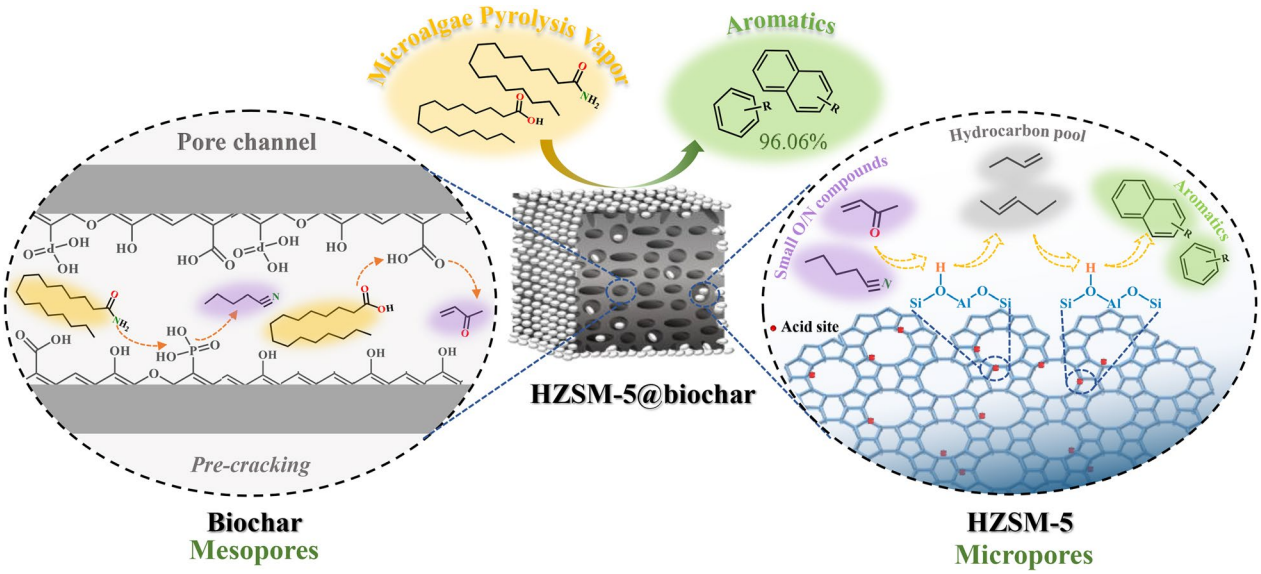

1 Introduction

Continuously increasing energy demand in today's world emphasizes the importance of developing renewable energy sources. Biofuel, as a renewable energy source that meets about 35% of energy demand in many developing countries and with global consumption risen to 13% (Hou et al. 2024), has been highlighted as a possible alternative to fossil fuels in various applications. Compared to lignocellulosic biomass, microalgae as a third generation biomass fuel has a high CO_2 fixation rate and short growth cycle and its cultivation does not need to occupy arable land (Bach and Chen 2017; Niu et al. 2022; Wang et al. 2019; Zhang et al. 2022). It mainly consists of lipids, proteins, and carbohydrates, which can be converted into bio-oil, biochar, and gas by pyrolysis. However, the presence of oxygen and nitrogen in microalgae leads to disadvantages such as high viscosity, instability, and low calorific value of the bio-oil (Kumar et al. 2022). At the same time, the nitrogen-containing compounds in bio-oils may also contribute to nitrogen-related pollution such as photochemical smog, ozone depletion, and greenhouse effect during combustion as a fuel source (Hou et al. 2024). Therefore, it is imperative to improve the quality of bio-oil through further deoxygenation and denitrogenation.

The application of catalysts facilitates the production of high-quality microalgae bio-oil by enhancing hydrocarbon selectivity and effectively removing oxygen and nitrogen (Nikkhah et al. 2020). Common catalysts include metal oxides, molecular sieves (such as HZSM-5), and biochar. Among these, metal oxides are prone to sintering and deactivation, and have weak removal capacity for nitrogenates. HZSM-5 zeolite can efficiently catalyze deoxygenation and denitrification, but its microporous structure is easily blocked by carbon deposits and ash metals, thus also facing the issue of easy deactivation (Ke et al. 2025). Biochar with a large specific surface area and a mesoporous structure showed the anti-coking potential (Liu et al. 2023), but it possesses fewer catalytic sites. Recent research has primarily focused on catalyst modification to enhance performance. For instance, Wu et al. demonstrated that metal-impregnated HZSM-5 significantly improved biomass deoxygenation and increased aromatic yield, while still facing rapid coking and catalyst deactivation when treating nitrogen-rich microalgal feedstocks (Wu et al. 2025). Meanwhile, biochar-based composite catalysts emerge as promising options due to their cost-effectiveness and abundant pore structures. Their abundant functional groups were beneficial for the adsorption of some macromolecules, thereby facilitating the further catalytic reforming. Research by Guo et al. (2025) showed that the Ni-Ce biochar catalyst achieved good deoxygenation activity in lignocellulosic pyrolysis, exhibiting high tar cracking activity (64.5% hydrocarbons) and good selectivity for monoaromatics (57.1%) (Guo et al. 2025). However, microalgae pyrolysis tends to produce large amounts of stubborn nitrogen-containing heterocycles such as pyrrole and indole, as

well as long-chain fatty acids (Leng et al. 2020). The fundamental understanding of how such composite catalysts promote simultaneous removal of oxygen and nitrogen heteroatoms during pyrolysis of complex biomass like microalgae remains limited. Specifically, detailed reaction pathways and the role of catalyst acid sites interacting with the biochar support remain poorly elucidated. Elucidating this mechanism is crucial for guiding the rational design and performance optimization of low-cost catalysts, as well as advancing the practical application of biochar-based catalysts. To address this knowledge gap, this study focuses on mechanistic investigations of catalytic pyrolysis using a composite catalyst (HZSM-5 coated biochar, HZSM-5@biochar). Its hierarchical pore structure optimizes mass transfer and alleviates coking-induced deactivation of HZSM-5. Simultaneously, the strong acidic sites of HZSM-5 compensate for the catalytic performance limitations of biochar. Thus, the deoxygenation and denitrogenation capacity of HZSM-5@biochar for the conversion of algal biomass deserves to be explored. Particularly, the conversion mechanism needs to be comprehensively revealed by investigating the conversion of the model components including protein, lipid, and carbohydrate. In addition, advanced strategies, such as in situ diffuse reflectance infrared Fourier transform spectroscopy (DRIFTS) and coke characterization were employed to help elucidate the mechanism.

Microalgae biomass exhibits a relatively high moisture content, and pre-treatment is required prior to pyrolysis. The conventional torrefaction pretreatment at temperatures of 200–300 °C requires high energy consumption and is ineffective (Dai et al. 2019). In recent years, wet torrefaction has attracted much attention as a pretreatment method that does not require the drying process. Wet torrefaction is a high-pressure thermal pretreatment method that operates in an inert environment at 150–260 °C in hot compressed water (Gan et al. 2018). This pretreatment method helps to pre-remove moisture and reduce the volume of microalgae. Compared to direct drying, the process of wet torrefaction can reduce energy consumption (Milanese et al. 2024). Additionally, during wet torrefaction, microalgal protein and carbohydrate undergo hydrolysis and decarboxylation reactions, enabling pre-deoxygenation and pre-denitrogenation of microalgae (Liu et al. 2022), which is beneficial for subsequent catalytic pyrolysis to produce high-quality bio-oil.

To date, although the catalytic pyrolysis of microalgae has been extensively studied, the mechanism of catalytic pyrolysis of microalgae for deoxygenation and denitrogenation to hydrocarbons has been rarely reported. In this study, HZSM-5@biochar was used for the catalytic pyrolysis of *Chlorella* pretreated with wet torrefaction. In addition, soybean protein, rapeseed oil, and glucose were selected as representatives of the three major components of algae (protein, lipids, and carbohydrates) for catalytic pyrolysis. Characteristic products from non-catalytic pyrolysis of *Chlorella* (1-nonadecene, hexadecanamide, n-hexadecanoic acid, isovaleraldehyde, and 1,3-dimethyl-2-imidazolidinone) were selected as pyrolysis model compounds for catalytic pyrolysis to investigate the catalytic pyrolysis pathway of algal biomass. X-ray Photoelectron Spectroscopy (XPS) and in situ DRIFTS analysis of the catalysts were performed to investigate the mechanism of deoxygenation and denitrogenation of *Chlorella*. Furthermore, the stability of HZSM-5@biochar was evaluated through cycling experiments and coke deposition studies.

2 Materials and method

2.1 Materials

Chlorella was purchased from Zhengzhou Best Food Additives Company, (Zhengzhou, China). Soy protein and glucose were purchased from Xilong Science Co, Ltd. (Shantou, China) and rapeseed oil was purchased from Dao Dao Quan Grain Oil Co, Ltd. (Yueyang, China). 1-nonadecene, hexadecanamide, n-hexadecanoic acid, isovaleraldehyde, and 1,3-dimethyl-2-imidazolidinone were all purchased from Shanghai Aladdin Biochemical Technology Co., Ltd. (Shanghai, China).

2.2 Wet torrefaction pretreatment

The wet torrefaction for *Chlorella* is as follows (Fig. 1a): A 100-mL batch reactor (Parr 4848 series-4590) was charged with 10 g *Chlorella* powder and 50 mL pure water at a 1:5 (w/v) solid–liquid ratio. Before heating, the gas tightness of the reactor was checked by holding about 1.0 MPa of N_2 for 10 min. The reactor was then heated at 4 °C min^{-1} to target temperatures (160 °C, 180 °C, 200 °C, 220 °C) and kept for 30 min with the stirrer set at 120 rpm. The resulting solid products were collected after cooling, filtering, drying, and grinding, and labeled as *Chlorella*-x (x = 160, 180, 200, 220).

The elemental composition was analyzed using an Elemental Analyzer (Elementar, Vario Macro Cube). The ash content was tested according to the National Standard of China (GB/T 28731–2012). Specific steps are detailed in supplementary material. The contents of oxygen (O) were calculated by difference. The detailed methods for determining the total lipid and protein content of the samples are provided in the supplementary material. Carbohydrate content was calculated by difference (Carbohydrates = 100% – Ash – Lipids – Proteins) (Su et al. 2022).

2.3 Catalyst preparation

The preparation of HZSM-5@biochar is as follows (Fig. 1b): biochar was prepared from soybean

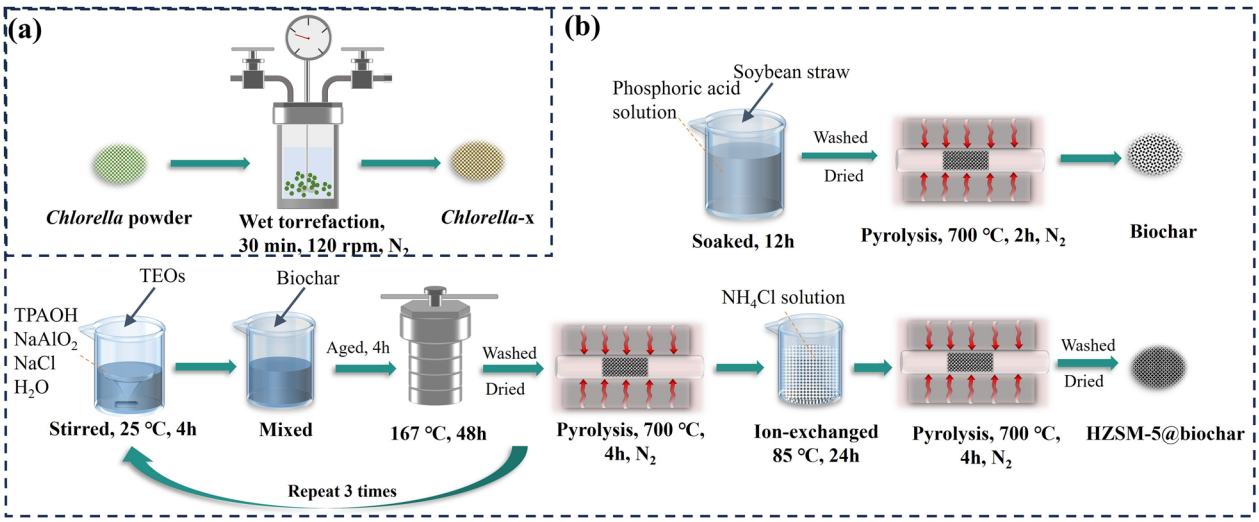

Fig. 1 Flowchart of **a** wet torrefaction pretreatment for *Chlorella* and **b** preparation of HZSM-5@biochar catalyst

straw—chosen for its ability to form a structurally robust carbon support compatible with the HZSM-5 coating (Dong et al. 2023)—by phosphoric acid impregnation (10 wt% H_3PO_4 solution, 12 h) followed by pyrolysis at 700 °C for 2 h under an inert atmosphere. The resulting biochar was washed to neutrality and dried. The HZSM-5@biochar was obtained by hydrothermal synthesis (Hu et al. 2024). The precursor gel was prepared by sequentially adding TEOS to a mixture of TPAOH, NaCl, $NaAlO_2$, and H_2O (molar ratios: 2.16:5.62:3.43:0.13:1000 for TPAOH:TEOS:NaCl:$NaAlO_2$:H_2O). Biochar (0.5 g) was added to the gel, aged at room temperature for 4 h, and then subjected to hydrothermal treatment at 167 °C for 48 h. This coating process was repeated three times. The solid product was calcined at 700 °C for 4 h under N_2 flow, followed by ion exchange with NH_4Cl solution. The product was calcined again for 4 h to obtain HZSM-5@biochar. The successful synthesis of HZSM-5@biochar composites was confirmed through X-ray diffraction, scanning electron microscopy (SEM), and EDS elemental mapping techniques (Fig. S1).

2.4 Catalytic pyrolysis experiments

The experiments were conducted using a fast pyrolyzer (Py-3030D, Shimadzu, Japan) coupled with gaschromatography-mass spectrometry (GC/MS, QP2010 SE, Shimadzu, Japan). Prior to pyrolysis, a microanalytical balance was used to precisely weigh (0.5 ± 10%) mg of biomass (m_1), which was then put in a sample cup. The catalyst was introduced at a 20:1 mass ratio relative to the feed. A quartz wool layer was placed to segregate the two components. The relatively high catalyst-to-feedstock ratio was due to the *ex-situ* catalysis mode, which required sufficient catalyst packing in the sample cup to ensure adequate vapor-catalyst contact and reaction. The sample cup, which contained feedstock, quartz wool, and catalyst, was weighed before and after the reaction, with the weights recorded as m_2 and m_3, respectively. Following helium purging of the thermal probe system, the sample cup was placed in the fast pyrolyzer and pyrolyzed by ramping to 500 °C at 600 °C min^{-1} and holding for 2 min. Evolving pyrolysis vapors were swept by helium into the GC/MS, which was operated using parameters described elsewhere (Fan et al. 2020). During this process, pyrolysis products were directly and online introduced into the GC/MS system for separation and identification. Therefore, this experimental procedure did not involve the collection and condensation of liquid bio-oil. The feedstock conversion was subsequently calculated using Eq. (1).

$$\text{Conversion (\%)} = \frac{m_2 - m_3}{m_1} \times 100 \quad (1)$$

To calculate the peak area yield (g^{-1} feedstock), the ratio of the measured peak area to the initial feedstock mass was adopted. The proportion of each compound's chromatographic area was used to calculate the product selectivity. Benzene, toluene, and xylene (BTX) yields were quantitatively analyzed using external standard procedures. At least three runs of each experiment were carried out, and the presentation of the data includes the mean and standard deviations (SD) values. Catalytic pyrolysis of soy protein, rapeseed oil, and glucose as algal components were also conducted following the aforementioned steps. A six-cycle stability test was conducted to evaluate the HZSM-5@biochar catalyst's durability. The procedure for each catalytic pyrolysis run was

identical to the detailed steps described above. After each reaction, the spent catalyst was recovered, regenerated by calcination at 700 °C for 2 h under a N_2 atmosphere, and then reused in the next cycle. HZSM-5 was used as a control. To quantitatively evaluate catalyst deactivation during cycling, the deactivation parameter D was introduced and calculated for each cycle n (n = 1, 2, …, 6) using the following equation: $D_n = X_n - X_6$, where X_n is the peak area yield of the product after cycling the catalyst for n times.

2.5 Conversion of oxygen- and nitrogen-containing functional groups of pyrolysis products

The changes in the chemical structure and elemental composition of the catalysts before and after use were investigated by XPS (Kratos AXIS SUPRA+, Japan) (Li et al. 2023) and Elemental Analyzer (Elementar, Vario Macro Cube), respectively. The conversion pathways of oxygen- and nitrogen-containing functional groups of pyrolysis products over different catalysts were probed using in situ DRIFTS (PerkinElmer Spectrum 3, USA). Specific procedures are detailed in the reference (Liu et al. 2024b), with the detection process conducted at 500 °C. The catalysts after the catalytic pyrolysis of 1-nonadecene (HZSM-5@biochar-1N), hexadecanamide (HZSM-5@biochar-H), n-hexadecanoic acid (HZSM-5@biochar-nH), isovaleraldehyde (HZSM-5@biochar-I), 1,3-dimethyl-2-imidazolidinones (HZSM-5@biochar-DI) were also examined with XPS.

2.6 Coke analysis

Based on thermogravimetric (TG) data, the coke yield was derived from the differential mass loss observed between the fresh and used catalysts. Additionally, the characteristics and structure of the coke were revealed using Raman spectroscopy and SEM. The specific characterization parameters are provided in elsewhere (Hu et al. 2024).

3 Results and discussion

3.1 Effect of wet torrefaction on catalytic pyrolysis of microalgae

In terms of the high peak area yield and chemical selectivity of aromatics, catalyst-to-feedstock ratio of 20:1 (Fig. S2) and pyrolysis temperature of 500 °C (Fig. S3) were chosen for the following catalytic pyrolysis runs. The impacts of wet torrefaction temperature and catalyst type on *Chlorella* pyrolysis were explored, using non-catalytic pyrolysis as the control. Table S1 lists detailed product selectivity for various catalyst-to-feed ratios and classifies the products into six categories: BTX, other mono-aromatics (other MAHs), polycyclic aromatic hydrocarbons (PAHs), oxygenates, nitrogenates, and aliphatics. Figure 2 displays the feedstock conversions, peak area yields and selectivity for each category. In the non-catalytic pyrolysis control experiments, the feedstock conversion decreased slightly with increasing wet torrefaction temperature (Fig. 2a), which was due to the increase in the mass density of the feedstock by the severe pretreating process (Wang et al. 2018). Simultaneously, the total peak area yield of each product exhibited an initial increase followed by a decline (Fig. 2b). This trend can be explained by the elimination of inorganic and volatile substances during wet torrefaction temperature elevation, which enhances energy density (Bach And Skreiberg 2016). However, excessively high temperatures result in elevated ash content and significant mass loss (Kostyniuk And Likozar 2024), causing a decrease in total peak area yield. In addition, among the non-catalytic pyrolysis products, almost no BTX were produced, and most were nitrogenates and oxygenates, whose total selectivity ranged from 80.74% to 84.29% (Fig. 2c). The selectivity for oxygenates decreased slightly with increasing wet torrefaction temperature, which is attributed to the preliminary deoxygenation of the feedstock during wet torrefaction pretreatment (supplementary material, Fig. S4). The product distribution from the catalytic pyrolysis with HZSM-5@biochar is shown in Figs. 1d–f. Due to the effect of wet torrefaction on the mass density of the feedstock, the feedstock conversion also showed a decreasing trend (Fig. 2d). As the wet torrefaction temperature increased, the total peak area yield and BTX peak area yield gradually increased and stabilized until 200 °C (Fig. 2e). Meanwhile, it can be observed from Fig. 2f that the selectivity of each product showed almost no change with increasing wet torrefaction temperature. However, the HZSM-5@biochar catalyst dramatically reduced the total selectivity of oxygenates and nitrogenates from 80.74–84.29% under non-catalytic conditions (Fig. 2c) to 2.14–6.34% (Fig. 2f), while enhancing aromatics selectivity to 90.94–97.84% (Fig. 2f). Notably, the catalytic of *Chlorella*-200 yielded a peak BTX selectivity of 83.24% (Fig. 2f) and yield of 94.64 mg g^{-1} (Fig. S5).

Compared to the control groups with HZSM-5 and biochar as the catalyst, the catalytic pyrolysis of HZSM-5@biochar possessed the highest feedstock conversion (92.83%, Fig. 2g), BTX peak area yield (3.20×10^{12} g^{-1}, Fig. 2h) and selectivity (83.24%, Fig. 2i), and the lowest content of oxygenates (1.87%) and nitrogenates (1.40%). In contrast, the biochar and HZSM-5 catalyzed pyrolysis products still contained significant amounts of nitrogenates and oxygenates. This observation correlates with the limited number of acidic sites of biochar (Eibner et al. 2017), which made it difficult to completely degrade oxygen-containing and nitrogen-containing compounds. Although HZSM-5 has strong acidity, its pore size is

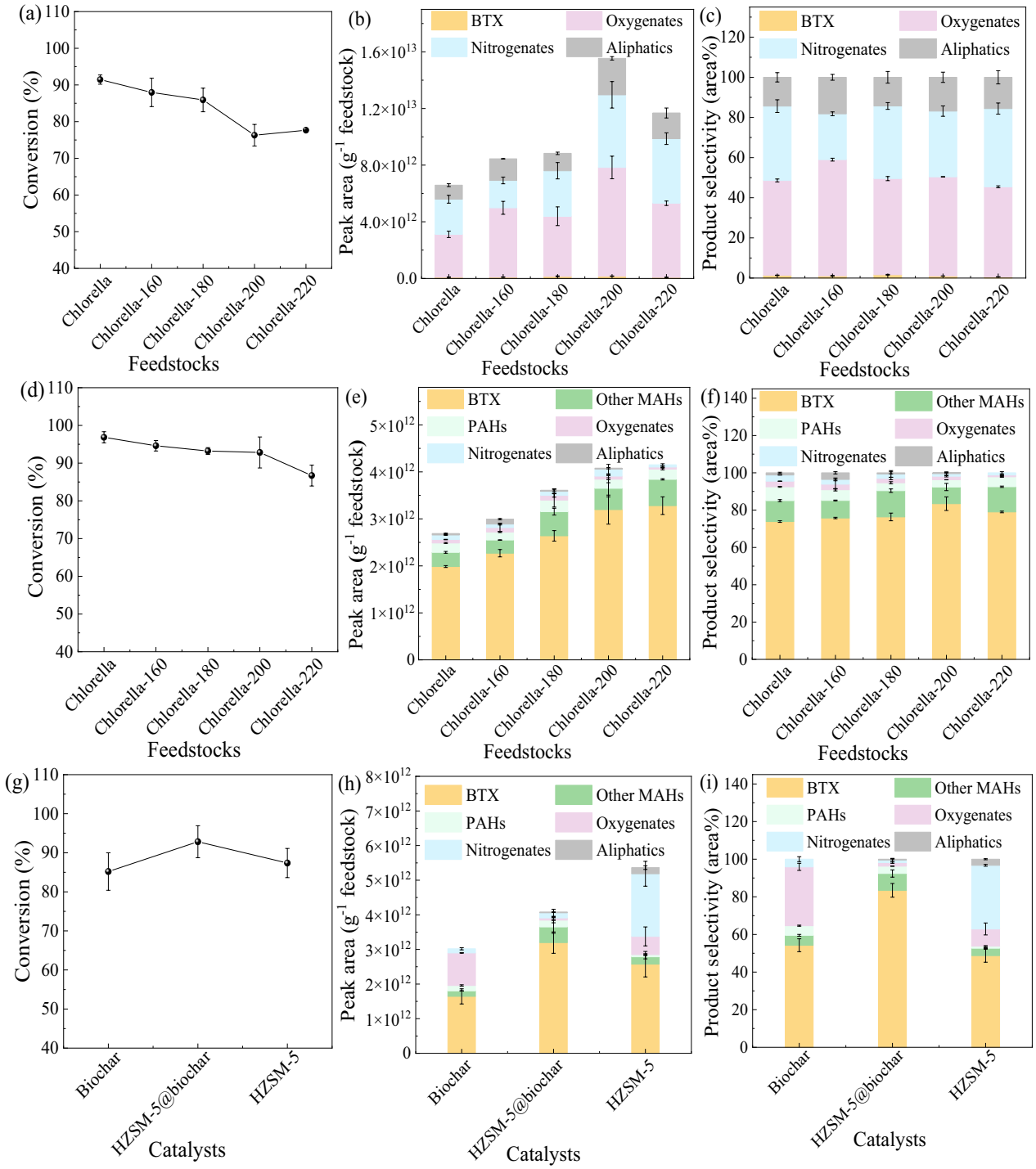

Fig. 2 Effect of wet torrefaction temperature and catalyst type on biomass pyrolysis: feedstock conversion, product peak area yield, and selectivity of organic compound groups for non-catalytic pyrolysis (**a**, **b**, **c**), HZSM-5@biochar-catalyzed pyrolysis (**d**, **e**, **f**) at varying wet torrefaction temperatures, and pyrolysis with different catalysts (**g**, **h**, **i**)

usually 5.5×5.1 Å (Hu et al. 2020), and once large molecules containing oxygen and nitrogen compounds generated from biomass pyrolysis enter into the pore channels, the HZSM-5 channels will be easily clogged, resulting in the deactivation of the catalyst (Wang et al. 2020). HZSM-5@biochar combined the advantages of both;

the biochar in the catalyst could initially adsorbed and decomposed the large molecule pyrolysis products, and the obtained small molecules were further converted into HZSM-5 to produce the aromatic products. This process reduced the possibility of large molecules entering and clogging the HZSM-5 channels, and thus the catalyst showed excellent catalytic performance along with satisfactory stability.

3.2 Mechanism of deoxygenation and denitrogenation of microalgae into aromatics

3.2.1 Catalytic conversion of model compounds

To explore the deoxygenation and denitrogenation mechanism in microalgae catalytic pyrolysis, three typical microalgae model compounds (soybean protein, rapeseed oil, and glucose) were employed as they can represent the primary components (proteins, lipids, and carbohydrates) of *Chlorella*. Among these, soy protein was selected to represent protein due to its amino acid composition, which closely resembles that of microalgae (Ziyue et al. 2023). Rapeseed oil was chosen to represent lipids, as its fatty acid profile is highly analogous to that of microalgal triglycerides (Suarez Ruiz et al. 2022). Monosaccharides (such as glucose) are the basic units of carbohydrates, linked by glycosidic bonds (Wang et al. 2017b). Simultaneously, corresponding catalytic pyrolysis experiments were carried out on these three model compounds under varying catalyst-to-feedstock ratios (5:1, 10:1, and 20:1). Figure 3 displays the product selectivity and peak area yields. Moreover, highly selectivity characteristic products from non-catalytic pyrolysis of *Chlorella*-200, including 1-nonadecene, hexadecanamide, n-hexadecanoic acid, isovaleraldehyde, and 1,3-dimethyl-2-imidazolidinone, were identified. These were subsequently subjected to catalytic conversion as model pyrolysis compounds. The obtained product distribution is presented in Fig. 4.

As depicted in Fig. 3, when the ratio of catalyst-to-feedstock was low (5:1), the catalytic pyrolysis of soybean protein produced nitrogenates and oxygenates as the prominent products, with selectivity of 46.32% and 33.76%, respectively. A further increase in the catalyst-to-feedstock proportion to 20:1 led to a significant decline in nitrogenates and oxygenates selectivity to 6.32% and 20.51%, respectively, while the BTX selectivity and peak area yield increased from 9.45% and 1.68×10^{11} g^{-1} to 59.50% and 5.08×10^{11} g^{-1}, respectively. It was because the presence of the catalyst resulted in

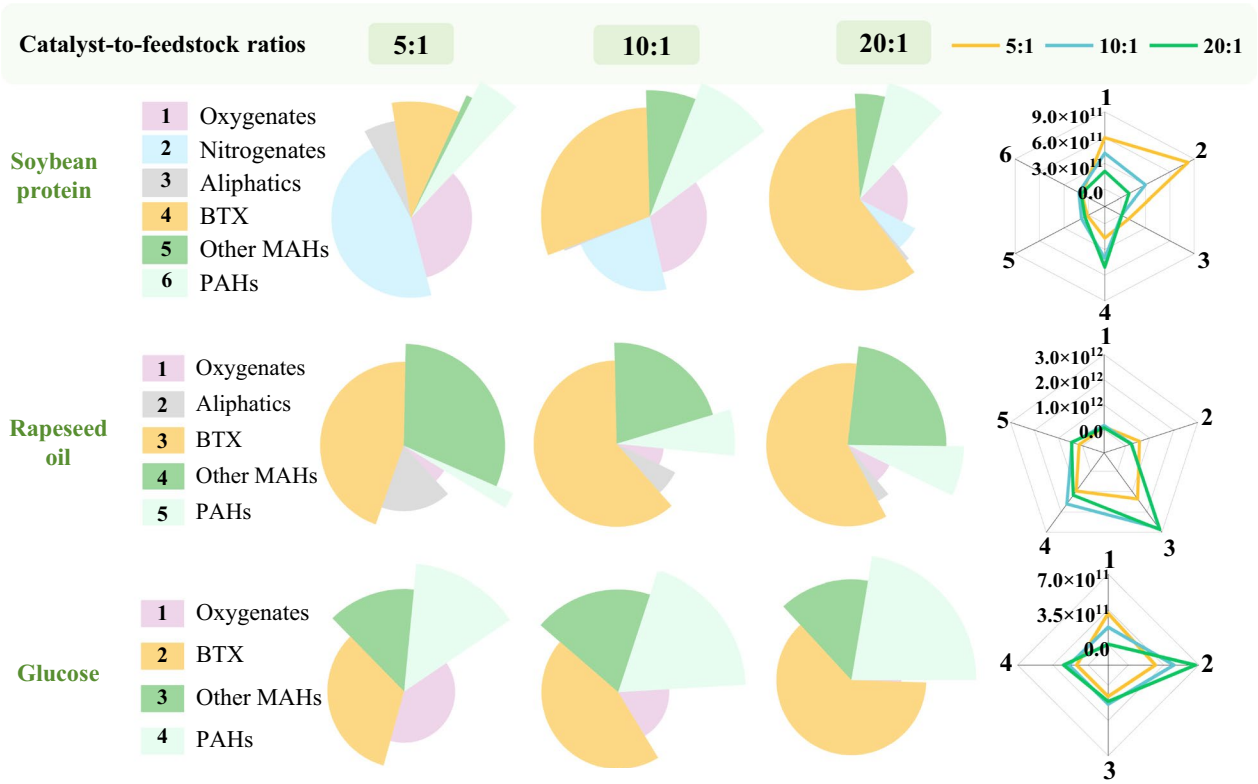

Fig. 3 Selectivity (pie chart) and peak area yield (radar chart) for soy protein, rapeseed oil, and glucose catalytic pyrolysis at 500 °C across various catalyst-to-feedstock ratios

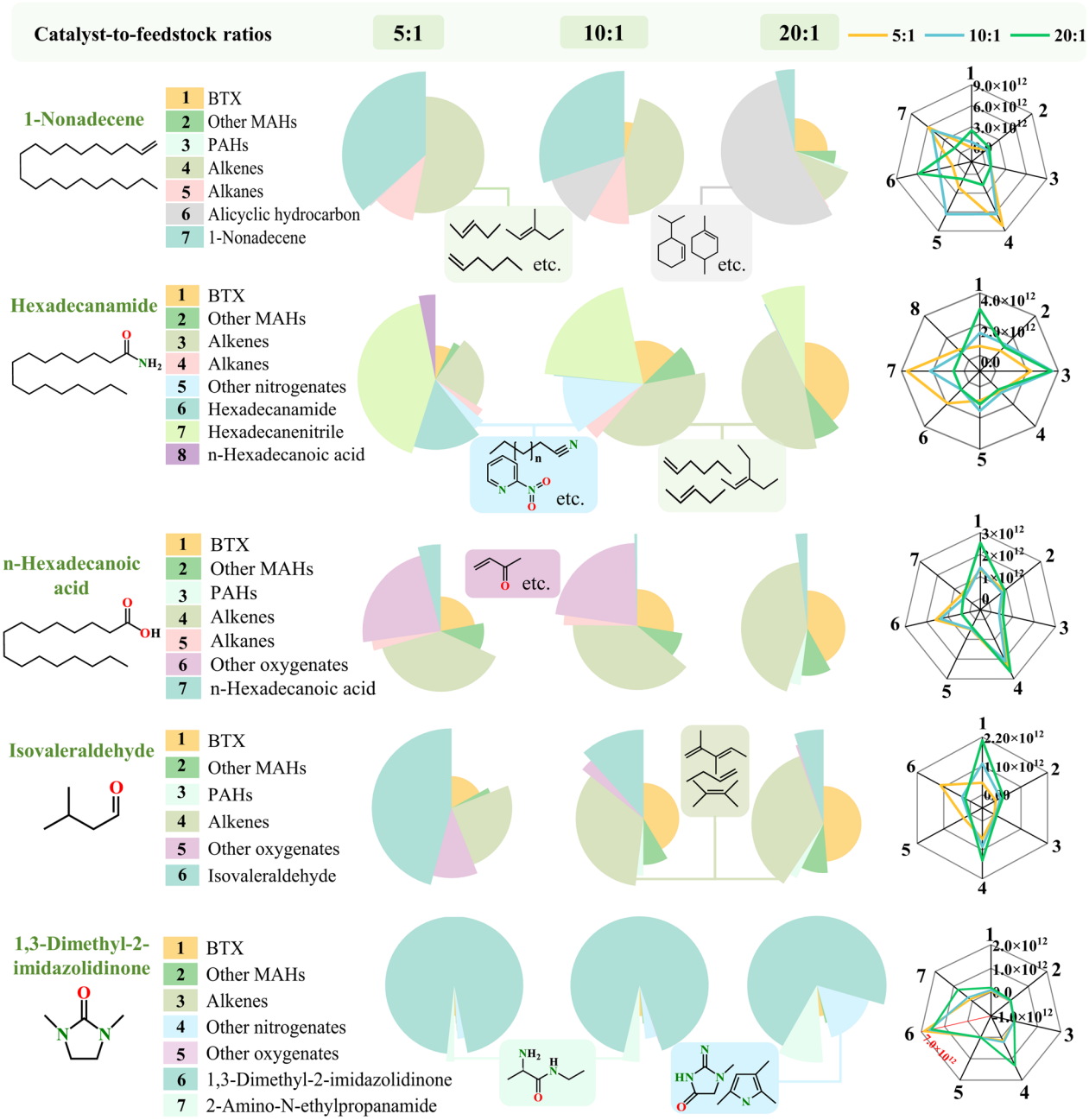

Fig. 4 Selectivity (pie chart) and peak area yield (radar chart) for 1-nonadecene, hexadecanamide, n-hexadecanoic acid, isovaleraldehyde, and 1,3-dimethyl-2-imidazolidinone catalytic pyrolysis at 500 °C across various catalyst-to-feedstock ratios

the denitrogenation of nitrogen-containing heterocycles by strong acid sites, thereby promoting aromatization. A similar trend was observed for rapeseed oil and glucose. Under the action of the catalyst, long-chain fatty acids produced from rapeseed oil were decarboxylated to form straight-chain alkenes, which subsequently converted to aromatics through cyclization and dehydrogenation (Cheng et al. 2017). Glucose was converted into furfural through dehydration, followed by Diels–Alder cycloaddition to form cyclic alkenes, and finally aromatized to benzene and toluene (Zhang et al. 2025). However, as shown in the radar chart, when the catalyst-to-feedstock ratio was 20:1, the BTX peak area yield of rapeseed oil (2.87×10^{12} g^{-1}) was significantly higher than that of soybean protein (5.08×10^{11} g^{-1}) and glucose (6.67×10^{11} g^{-1}). This may be because rapeseed oil had a

relatively high hydrogen content, and its oxygen elements mainly existed in the form of ester groups, making the deoxygenation pathway simple. During the soybean protein pyrolysis, some nitrogen could be escaped as HCN, causing carbon loss and poisoning the acid sites, thereby inhibiting aromatization efficiency (Guo et al. 2024). During the catalytic pyrolysis of glucose, PAHs with a selectivity of 22.33% (Fig. 3) were produced, which blocked the catalyst pores and impaired catalytic performance. In addition, it is noteworthy that aliphatics existed in the catalytic pyrolysis of soybean protein and rapeseed oil, and their selectivity tended to decrease with the increase of the catalyst addition, indicating the crucial intermediate product during the catalytic pyrolysis process.

During the catalytic pyrolysis of 1-nonadecene at a catalyst-to-feedstock ratio of 5:1, the product with the highest selectivity was alkenes (53.11%), followed by 1-nonadecene (36.56%) and alkane (10.00%) (Fig. 4). This result corresponds to the left part of Path 1 in Fig. 5, indicating that the catalyst promoted the cracking of 1-nonadecene, resulting in lighter short-chained olefins and paraffins, such as 2-pentene, 2-ethyl-2-butene, and 1-hexene. As the catalyst-to-feedstock ratio rose to 20:1, 1-nonadecene was further consumed, and new products (alicyclic hydrocarbons and BTX) were produced, whose selectivity reached 54.61% and 24.86%, respectively. This shift aligns with the subsequent pathway depicted in Fig. 5 (Path 1), originating from alkene and alkane intermediates: alkenes and alkanes underwent cyclization to form alicyclic hydrocarbons, followed by further aromatization to form BTX (Vogt et al. 2023). In addition, bimolecular reactions (e.g., cross-linking, Diels–Alder reaction, etc.) occurred between alkenes, alkynes, and/or dienes to form (poly) aromatics (Abbas-Abadi et al. 2023).

During the catalytic conversion of hexadecanamide, depicted in Fig. 4, hexadecanenitrile was the primary product, exhibiting a high selectivity of 41.94% (catalyst-to-feedstock ratio of 5:1). However, as the catalyst ratio further increased, the hexadecanenitrile selectivity gradually decreased. As shown in Path 2 of Fig. 5, this could be attributed to the dehydration of hexadecanamide, forming the hexadecanenitrile intermediate (Anand et al. 2017), after which this substance underwent further cracking to form other short-chain nitriles. In addition, it has been reported that the cyclization of amide/amine forms nitriles and N-heterocyclics (Tang et al. 2021), among which nitriles would be further converted to alkanes and alkenes (Fig. 5, Path 2), and finally produced aromatics after a series of

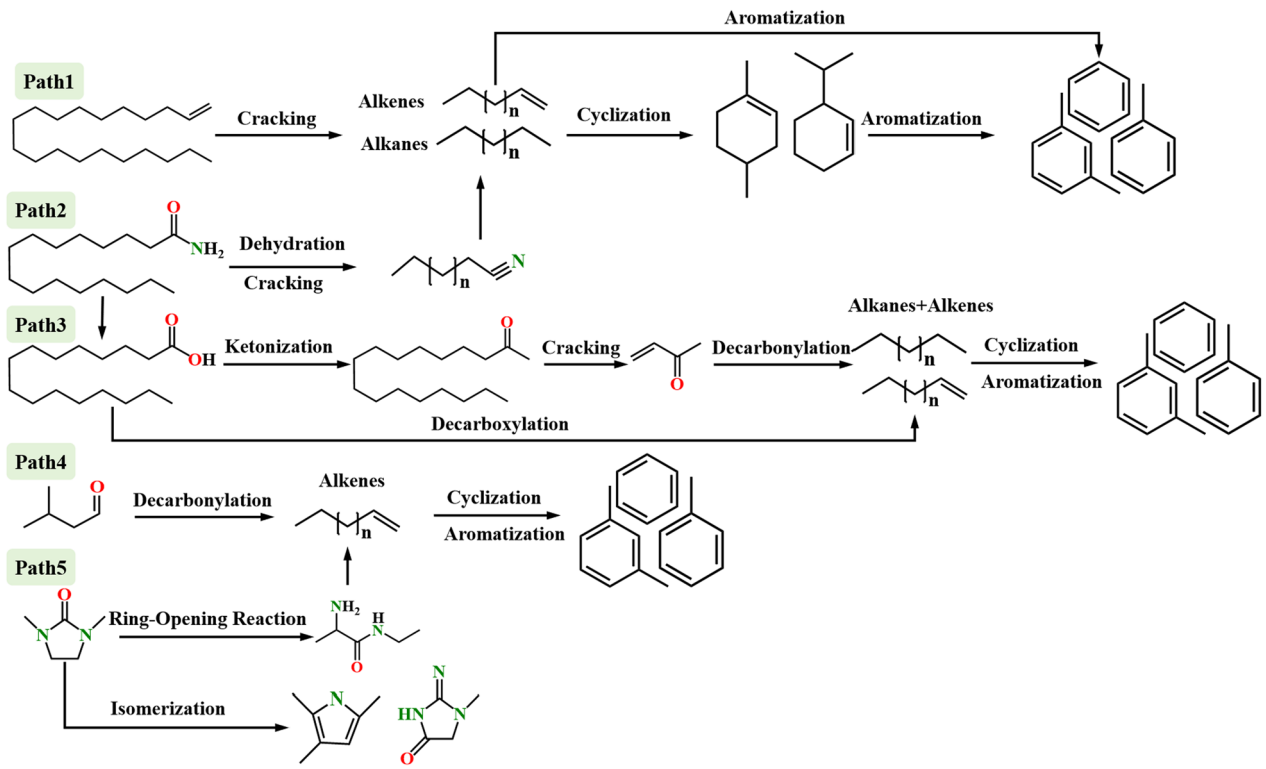

Fig. 5 Aromatic conversion pathways of 1-nonadecene, hexadecanamide, n-hexadecanoic acid, isovaleraldehyde, and 1,3-dimethyl-2-imidazolidinone

reactions (Fig. 5, Path 1). During the reaction process, other nitrogenates (e.g., heptanonitrile, octanenitrile and 2-nitropyridine) (Fig. 4) functioned as nitrogenous intermediates. Their concentrations initially increased and subsequently decreased gradually as these intermediates were consumed in further reactions.

The products from the pyrolysis of n-hexadecanoic acid in the presence of catalyst contained 23% of other oxygenates (Fig. 4), among which methyl vinyl ketone was remarkable. As shown in Path 3 of Fig. 5, this is presumed to result from the ketonization and cracking of n-hexadecanoic acid (Wang et al. 2017a). As the catalyst-to-feedstock ratio gradually increased to 20:1, no other oxygenates were present in the products, while the selectivity and peak area yields of alkenes (42.9% and 2.59×10^{12} g^{-1}) and BTX (41.89% and 2.53×10^{12} g^{-1}) were most dominant (Fig. 4). This phenomenon might stem from the further decarbonylation of oxygen-containing compounds like methyl vinyl ketone, generating alkanes and alkenes as intermediates (Fig. 5, Path 3). These intermediates were then efficiently converted to aromatics via subsequent aromatization catalyzed by HZSM-5@biochar. (Tian et al. 2022). Catalytic pyrolysis of isovaleraldehyde revealed, as shown in Fig. 4, a gradual decrease in its selectivity from 45.77% to 4.99% with increasing catalyst loading. Concurrently, the content of alkenes progressively increased. These trends indicate that the conversion pathway of isovaleraldehyde is analogous to that of ketones. As described in Path 4 of Fig. 5, isovaleraldehyde first dehydrated in the zeolite channel of the catalyst to produce unsaturated olefins (hydrocarbon pools), and then the aromatic ring structure was constructed by the Diels–Alder reaction (Liu et al. 2024a).

The extent of catalytic conversion of 1,3-dimethyl-2-imidazolidinone was dramatically lower than that of the other model compounds. Even at the highest catalyst loading (20:1), 71.28% of the feed remained unconverted, which was determined by the high thermal stability of the heterocyclic nitrogen contained in the substance (Zheng et al. 2020). Nevertheless, the selectivity and peak area yields of 2-amino-N-ethylpropanamide, BTX, and other oxygenates gradually rose with rising catalyst loading. This could be attributed to the attack of H radicals generated during catalytic pyrolysis on the N site of the heterocyclic N. This attack weakened the C–N bond in the imidazolidone ring, leading to ring-opening of the heterocycle and promoting the conversion of 1,3-dimethyl-2-imidazolidone to 2-amino-N-ethylpropanamide (Gu et al. 2019). Subsequently, the intermediate underwent C–N bond cleavage and C–C bond cleavage to yield small-molecule alkenes. These alkenes ultimately converted into aromatics via aromatization. This reaction pathway is elucidated in Fig. 5 (Path 5). Meanwhile, 1,3-dimethyl-2-imidazolidinone isomerized to produce other nitrogenates such as 2,3,5-trimethyl-1H-pyrrole and creatinine (Costil et al. 2017).

3.2.2 Conversion pathway of oxygen- and nitrogen-containing functional groups

Understanding the oxygen- and nitrogen-containing functional groups on HZSM-5@biochar is the key to elucidating the catalytic conversion mechanism of microalgae. Their characteristics in the catalyst were firstly detected by XPS. Subsequently, elemental analysis assessed the macroscopic changes in the elemental composition of the catalyst before and after the reaction. The conversion pathways of these functional groups were subsequently tracked using in situ DRIFTS spectroscopy.

XPS analysis provided direct evidence for understanding the surface chemistry of catalysts and its evolution during reactions. Firstly, the comparative XPS survey spectra of HZSM-5@biochar and biochar (Fig. S6) revealed that HZSM-5@biochar exhibited characteristic Si 2p and Al 2p peaks originating from the zeolite framework structure of HZSM-5 (Oseke et al. 2021), which were absent in the pristine biochar. Simultaneously, compared to biochar, the intensity of the C 1 s peak was reduced in HZSM-5@biochar, while the O 1 s intensity increased. These changes could be attributed to HZSM-5 coating the biochar support within the catalyst, introducing significant Si, Al, and O elements while suppressing the C signal from the biochar. The successful synthesis of the HZSM-5@biochar catalyst was thus confirmed (consistent with prior XRD and SEM characterization), establishing the foundation for subsequent studies. More importantly, changes in the chemical structure of catalysts before and after catalyst action were analyzed using XPS. Seven and three Gaussian and Lorentzian peaks were used to fit the C 1s and N 1s curves (Ayiania et al. 2020a; Li et al. 2023, 2017; Shi et al. 2016), respectively, and representative deconvolution C 1s spectra and N 1s spectra are shown in Fig. S7 and Fig. S8. Table S2 and Table S3 list the typical functional groups for C 1s spectra and N 1s spectra, respectively. The content of each functional group in the C 1 s spectrogram is listed in Table 1. It can be observed that the decrease in the peak II (associated with aromatic C–C/C–H bonds) intensity of all spent catalysts implied a reduction in the aromatic carbon structures exposed on the catalyst surface. Since the aromatic ring system serves as an active site (Li et al. 2023), this suggested that some active sites may have been covered after catalyst use. Meanwhile, the intensities of $C–C_{low}$ and $C–C_{high}$, which separately represent disordered and defective carbon structures, were enhanced, indicating that the catalyst produced defects

Table 1 XPS C 1 s deconvolution results of fresh and spent catalysts (peak composition, %)

Peak	I	II	III	IV	V	VI	VII
	$C–C_{low}$	$C–C_{primary}$	$C–C_{high}$	C–O	C=O	C(O)–O	π – π*
HZSM-5@biochar	8.18	38.99	21.72	12.19	10.12	6.56	2.24
HZSM-5@biochar-1N	8.56	41.95	22.14	14.56	9.11	2.79	0.89
HZSM-5@biochar-H	12.92	29.33	22.92	16.03	8.69	4.77	5.34
HZSM-5@biochar-nH	14.67	28.45	25.45	14.70	10.23	5.47	1.03
HZSM-5@biochar-I	29.10	36.97	18.39	5.53	2.62	6.35	1.05
HZSM-5@biochar-DI	9.77	30.44	28.99	12.14	8.75	6.11	3.79

HZSM-5@biochar-1N, HZSM-5@biochar-H, HZSM-5@biochar-nH, HZSM-5@biochar-I, and HZSM-5@biochar-DI represent catalysts obtained from catalytic pyrolysis of 1-nonadecene, hexadecanamide, n-hexadecanoic acid, isovaleraldehyde, and 1,3-dimethyl-2-imidazolidinones, respectively

Table 2 XPS N 1 s deconvolution results of fresh and spent catalysts (peak composition, %)

Peak	I	II	III
	C=N–C	C–(NC)–C	O=N–C
HZSM-5@biochar	27.22	40.91	31.88
HZSM-5@biochar-DI	46.10	22.09	31.81
HZSM-5@biochar-H	36.09	27.49	36.43

HZSM-5@biochar-H and HZSM-5@biochar-DI represent catalysts obtained from catalytic pyrolysis of hexadecanamide and 1,3-dimethyl-2-imidazolidinones, respectively

Table 3 Elemental composition (CHNS) of the HZSM-5@biochar before and after reaction with different model compounds

Sample	N (%)	C (%)	H (%)	S (%)
HZSM-5@biochar	0.36	17.62	0.86	0.04
HZSM-5@biochar-1N	0.39	19.11	0.92	0.03
HZSM-5@biochar-H	0.42	19.84	0.83	0.00
HZSM-5@biochar-nH	0.40	20.77	0.85	0.04
HZSM-5@biochar-I	0.41	22.25	0.96	0.05
HZSM-5@biochar-DI	0.61	20.96	0.91	0.03

HZSM-5@biochar-1N, HZSM-5@biochar-H, HZSM-5@biochar-nH, HZSM-5@biochar-I, and HZSM-5@biochar-DI represent catalysts obtained from catalytic pyrolysis of 1-nonadecene, hexadecanamide, n-hexadecanoic acid, isovaleraldehyde, and 1,3-dimethyl-2-imidazolidinones, respectively

when interacting with the model compounds (Ayiania et al. 2020a). Additionally, compared with fresh HZSM-5@biochar, the intensities of C=O and C(O)–O in the spent catalysts were reduced in different degrees, which could be ascribed to the fact that the catalytic process promoted the oxygen-containing functional groups reaction. It was also reported that the steady disappearance of unstable oxygen-containing functional groups indirectly promoted the condensation reaction of aromatic hydrocarbon (Du et al. 2024).

The N 1 s spectra are partitioned into 3 peaks: pyridinic (Peak I), graphitic (Peak II), and N-oxide (Peak III) (Ayiania et al. 2020a; Shi et al. 2016), and the intensities of peaks are presented in Table 2. A notable reduction in the Peak II intensities of HZSM-5@biochar-DI and HZSM-5@biochar-H was observed relative to HZSM-5@biochar. The graphitic nitrogen represented by this peak is strongly associated with the acidic sites (Shi et al. 2016); thus, the reduction of its intensity may be caused by the structural change of graphitic nitrogen with the action of acidic sites. Besides, the increases in peak I and peak III intensities may be due to the transformation of graphitic nitrogen. Some pyrrolic nitrogen may be produced in this process. It can be decomposed by a disproportionation reaction to produce stable structures (e.g. pyridinic nitrogen, graphitic nitrogen) and contribute to the production of NH_3, HCN, and NO.

Elemental analysis was employed to investigate changes in the elemental composition of HZSM-5@biochar after pyrolysis using different model compounds. As shown in Table 3, the N content in the HZSM-5@biochar increased significantly (from 0.36% to 0.61%) following catalytic pyrolysis using 1,3-dimethyl-2-imidazolidinone as the feedstock. This was due to the stable N-heterocyclic structure in this compound, which was difficult to fully convert on the catalyst, leading to nitrogen retention. This finding not only corroborated the significant enhancement of the pyridine nitrogen signal in the N 1 s spectra (Table 2) but also aligned with the phenomenon observed in Fig. 4, where 1,3-dimethyl-2-imidazolidinone exhibited poor convertibility. Interestingly, hexadecanamide, also a nitrogen-containing compound, exhibited only a modest increase in nitrogen content (from 0.36% to 0.42%). This might be attributed to the highly efficient denitrogenation of amide functional groups on the HZSM-5@biochar, which prevented nitrogen deposition on the catalyst surface. Furthermore, compared to fresh HZSM-5@biochar, all spent catalysts showed increased C and H content. This indicated that hydrocarbon deposition (coking) occurred during the catalytic pyrolysis process.

To deeply explore the catalytic conversion mechanism of O and N-containing functional groups of primary pyrolysis compounds on HZSM-5@biochar, isovaleraldehyde and propionamide were selected for in situ DRIFTS spectra determination, and HZSM-5 was used as the control.

As presented in Figs. 6a and b, at the beginning of the detection (T = 250 s), peaks appeared only at around 1730 cm^{-1} (peak 2), 2710 cm^{-1} (peak 3), and 2950 cm^{-1} (peak 6), which resulted from the C=O stretching vibration, C–H stretching vibration of aldehydes, and asymmetric stretching vibration of aliphatic-CH_3 (Wang et al. 2017c; Yu et al. 2023), respectively, indicating the structure of isovaleraldehyde. With further reaction of isovaleraldehyde, a broad peak (peak 7) representing OH stretching was produced at 3450 cm^{-1} at 2100 s, indicating the formation of abundant bridges of hydrogen (Orrego-Restrepo et al. 2022), and its intensity gradually declined over time. This phenomenon is possibly because the C=O group of isovaleraldehyde was attacked by activated H atoms of HZSM-5@biochar, converting it into an alcohol intermediate (isoamyl alcohol) which subsequently underwent further reactions. In addition, new peaks also appeared at near 1500 cm^{-1} (peak 1), 2850 cm^{-1} (peak 4), and 2870 cm^{-1} (peak 5). Peak 1 represented the aromatic C=C stretching vibration, while peaks 4 and 5 referred to the symmetric vibration of $–CH_2$ and $–CH_3$ in aliphatic hydrocarbons (Yu et al. 2023), which suggested that the resulting alcohols were most likely to be further deoxygenated to hydrocarbons and ultimately converted to aromatics (Fig. 6c). In contrast, under the catalytic effect of HZSM-5, peak 7 was of low intensity and a new peak (peak 8) appeared at about 1600 cm^{-1} (Fig. 7b), which can be attributed to the conjugated C=O stretching vibration (Yu et al. 2023). It suggested that HZSM-5, different from HZSM-5@biochar, tended to convert isovaleraldehyde to butenal with conjugated structures and further to hydrocarbons. Moreover, peak 1 never appeared during the reaction on HZSM-5, verifying that aromatics were not produced during the process. The following reasons could explain the difference in the catalytic actions of the two catalysts. When isovaleraldehyde entered the HZSM-5@biochar, it preferred to react with the acidic sites of the biochar due to the adsorption and the mesoporous structure of the biochar in the catalyst and was more inclined to break the relatively unstable C=O bonds to be transformed into isoamyl alcohol (Fig. 6c). In the HZSM-5 catalyst, the stable C–C bond could be broken due to its strong acidity, but the easy deactivation of HZSM-5 made it difficult to reach the step of isovaleraldehyde conversion to generate aromatics (Fig. 7c).

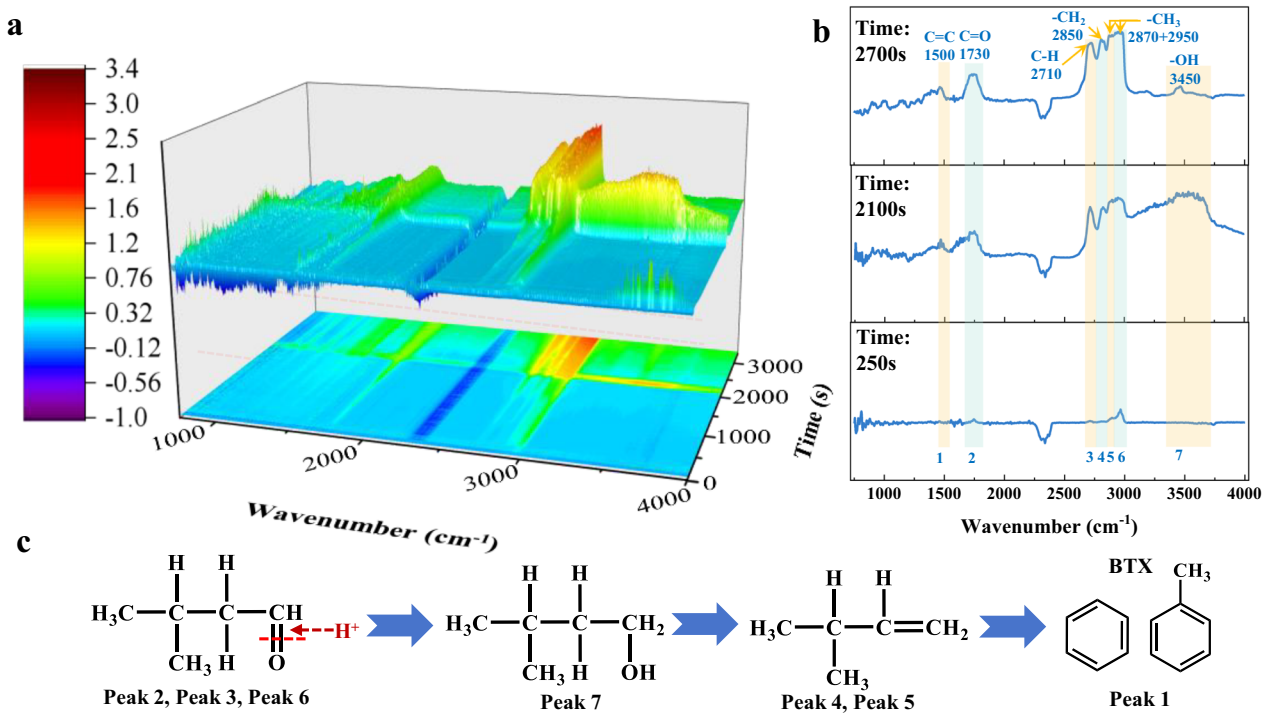

Fig. 6 Results of isovaleraldehyde catalyzed by HZSM-5@biochar: **a** in situ DRIFTS spectra at different times, **b** in situ DRIFTS spectra at time = 250 s, time = 2100s, and time = 2700 s, **c** catalytic conversion pathway of isovaleraldehyde

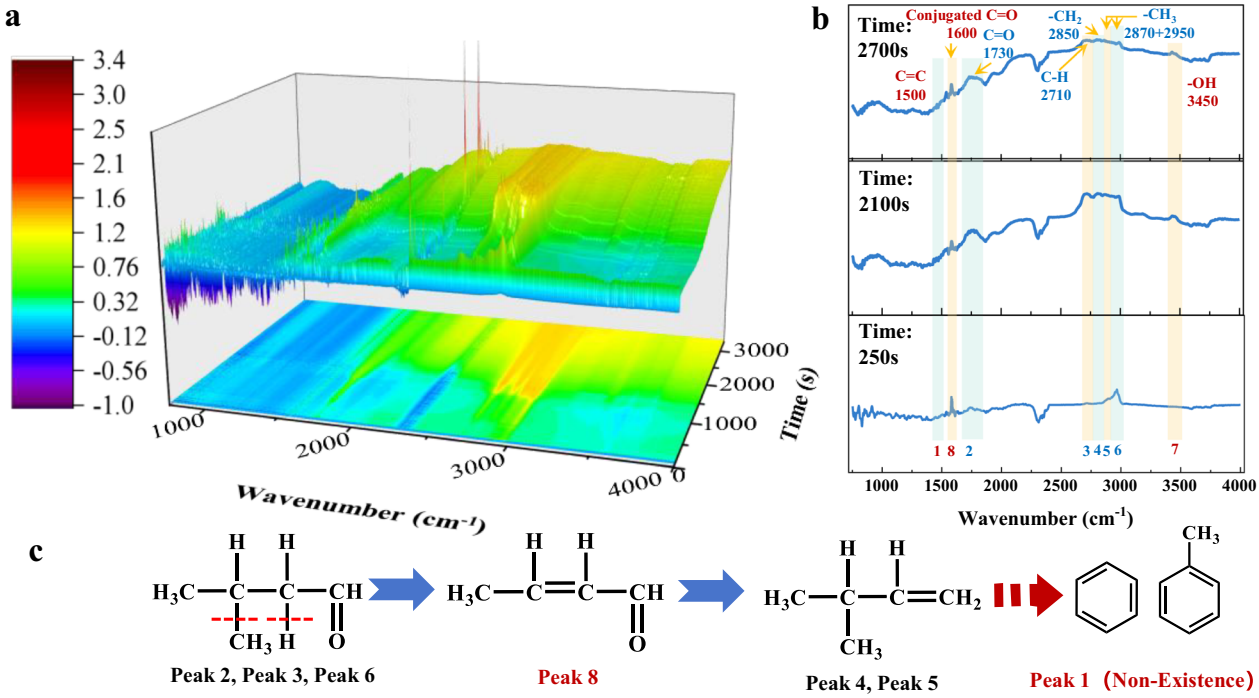

Fig. 7 Results of isovaleraldehyde catalyzed by HZSM-5: **a** in situ DRIFTS spectra at different times, **b** in situ DRIFTS spectra at time = 250 s, time = 2100s, and time = 2700 s, **c** catalytic conversion pathway of isovaleraldehyde

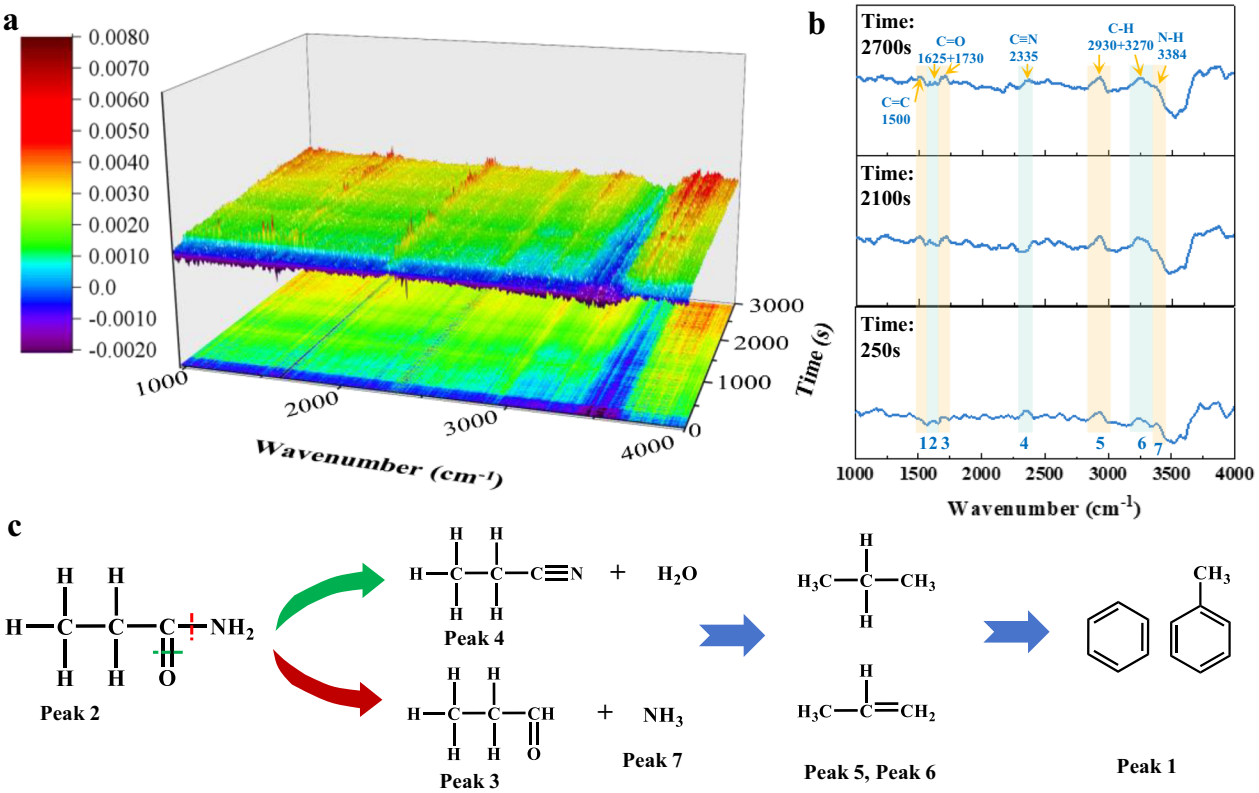

Fig. 8 Results of propionamide catalyzed by HZSM-5@biochar: **a** in situ DRIFTS spectra at different times, **b** in situ DRIFTS spectra at time = 250 s, time = 2100s, and time = 2700 s, **c** catalytic conversion pathway of propionamide

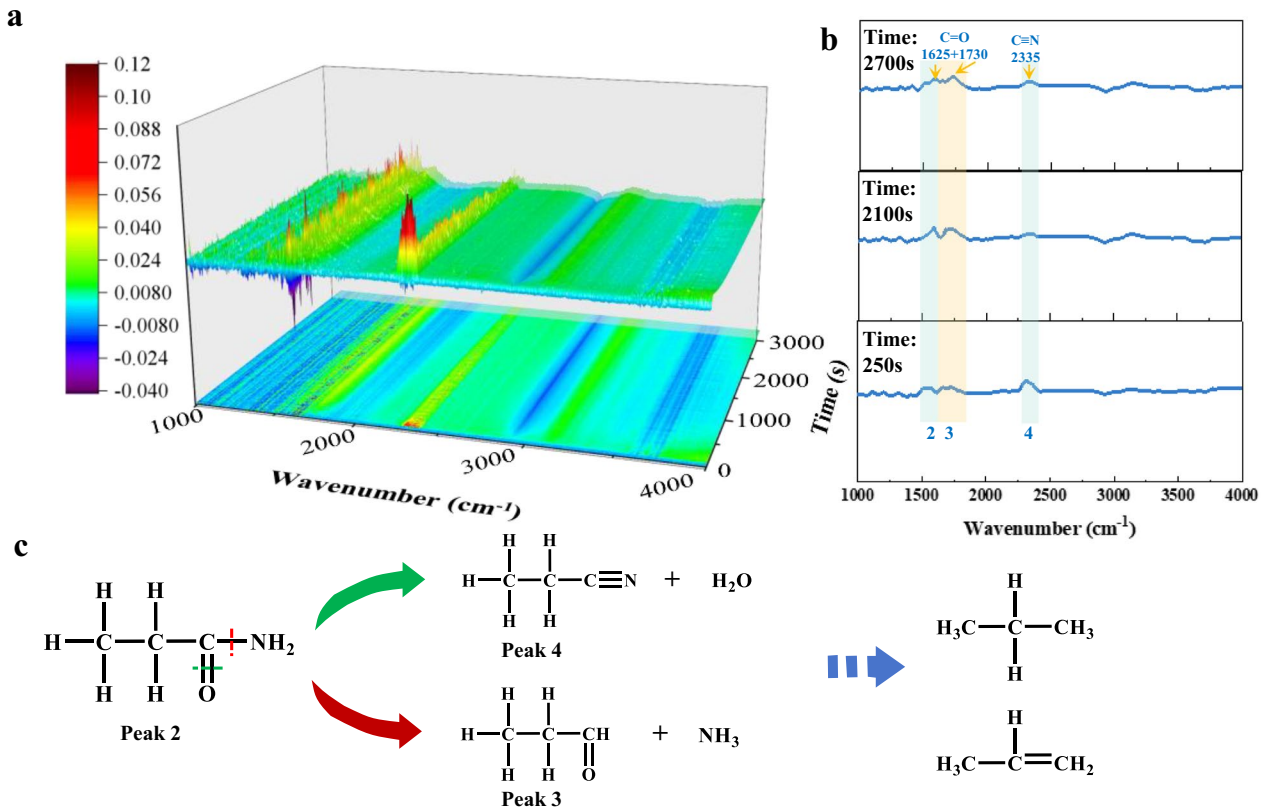

Fig. 9 Results of propionamide catalyzed by HZSM-5: **a** in situ DRIFTS spectra at different times, **b** in situ DRIFTS spectra at time = 250 s, time = 2100s, and time = 2700 s, **c** catalytic conversion pathway of propionamide

Figures 8 and 9 present the in situ DRIFTS spectra from the catalysis of propionamide. As shown in Fig. 8, the stretching vibration of C=C in aromatics was detected at 1500 cm^{-1} (peak 1). The adsorption bands at 1625 cm^{-1} (peak 2) and 1730 cm^{-1} (peak 3) were ascribed to the C=O stretching vibrations of amides and aldehydes, respectively (He et al. 2022). In addition, the stretching vibration of C≡N was observed at 2335 cm^{-1} (peak 4) (Figueiredo et al. 2016), indicating the presence of nitrile. Its intensity first decreased and then increased with time. The first decrease could be because the nitrile was further reacted during the reaction process to reduce its content, and the second increase could be explained by the continuously production of nitrile with the entry of propionamide. The peaks at near 2930 cm^{-1} (peak 5), 3270 cm^{-1} (peak 6), and 3384 cm^{-1} (peak 7) were derived from the methyl symmetric C–H stretching vibration in alkanes, C–H stretching in alkynes, and the stretching vibration of N–H in NH_3, respectively (Chhabra et al. 2020). The intensity of these peaks gradually rose with time, indicating that hydrocarbons as well as NH_3 were produced during the conversion of propionamide. Therefore, the catalytic conversion of propionamide under the action of HZSM-5@biochar can be hypothesized as follows (Fig. 8c): propionamide was first converted to nitrile by deoxygenation or aldehydes by denitrogenation, and then further hydrocarbons, such as alkanes, and finally aromatics as the end products. The result under the catalytic action of HZSM-5 is illustrated in Fig. 9, in which there were only peaks 2, 3 and 4, showing that propionamide may only be converted to nitrile and aldehyde under the catalytic action of HZSM-5, and then it would not be further reacted. The intensity of peak 4 was high at the beginning, but decreased rapidly, which may be due to the instantaneous combination of propionamide and the catalytic site of HZSM-5 to produce nitrile, but the site failed rapidly and no more new groups were produced. Meanwhile, the air flow took away part of the C≡N group and made the peak 4 intensity decreased.

3.2.3 HZSM-5@biochar catalytic microalgae pyrolysis mechanism

The catalytic pyrolysis pathway of microalgae is shown in Fig. 10. Microalgae primarily consist of carbohydrates, lipids, and proteins, which undergo gradual reactions at high temperatures. Carbohydrates underwent

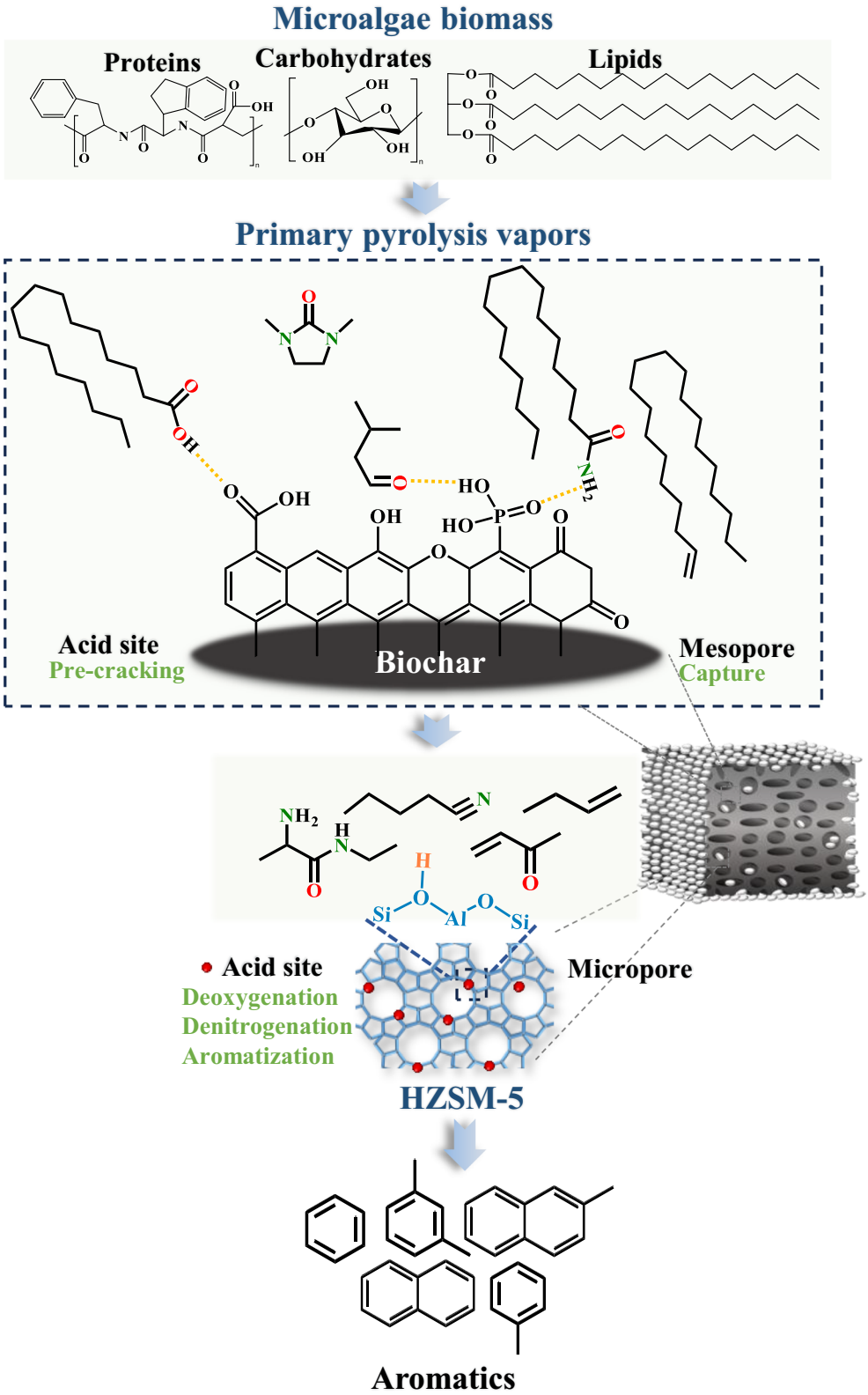

Fig. 10 Schematic illustration of the catalytic conversion of microalgae into aromatics

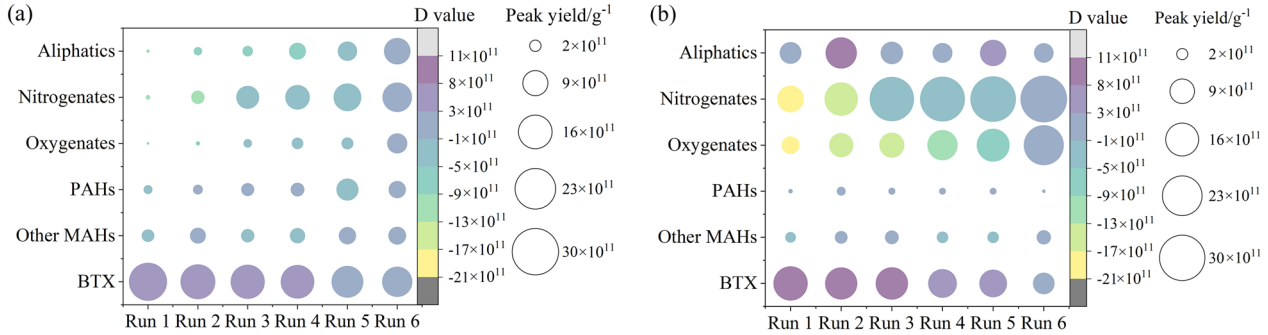

Fig. 11 Results of cycling experiments of **a** HZSM-5@biochar and **b** HZSM-5

depolymerization, dehydration, decarboxylation, and cleavage, forming oxygenates (such as alcohols, furans, phenols, carboxylic acids, ketones, and aldehydes). Lipids were decomposed through dehydration, decarboxylation, decarbonylation, and fatty acid formation. The resulting fatty acids were further decomposed into long-chain hydrocarbons, acids, and esters (Zhang et al. 2022). Proteins were primarily decomposed through polymerization, decarboxylation, dehydration, and deamination reactions, leading to N-heterocyclic compounds, nitriles, and amides. Additionally, nitrogen-containing heterocyclic compounds (e.g., pyrroles, indoles, pyridines) were produced in the Maillard reaction (Niu et al. 2022). Consequently, the primary pyrolysis vapors generated by microalgal pyrolysis consisted of the above-mentioned large-molecule oxygenates and nitrogenates.

The subsequent stage involved contacting the primary vapors with a catalyst bed of HZSM-5@biochar. Initially, the biochar component in the catalyst utilized its exceptional adsorption properties and mesoporous structure to adsorb and retain these primary products. This process led to the accumulation of most large-molecular compounds within the mesoporous structure of the biochar. Since the biochar was activated with phosphoric acid, its surface retained abundant functional groups (such as –COOH, quinone groups, $–PO_3H$, etc.), which could pre-crack large-molecule oxygenates and nitrogenates. For large-molecule oxygenates such as n-hexadecanoic acid, the catalytic pyrolysis process produced small-molecule ketone intermediates (Path 1 in Fig. 5). This occurred because the COOH groups on the biochar surface adsorbed n-hexadecanoic acid via hydrogen bonding (Dong et al. 2024), and the O–H bond broke to release H^+. The released proton then protonated the carboxyl group, forming the metastable cation $R\text{-}COOH_2^+$. Two adsorbed n-hexadecanoic acid molecules condensed at adjacent acidic sites to form ketone intermediates (Pham et al. 2013), which then decomposed into small-molecule ketones. Long-chain hydrocarbons such as 1-nonadecene had a terminal double bond that was adsorbed by electron-deficient quinone groups. This adsorption caused polarization of the double bond, forming a carbenium ion. The carbenium ion underwent β-cleavage to yield short-chain alkenes and alkanes (Zuo et al. 2025). For large nitrogenates such as hexadecanamide, the $–PO_3H$ functional groups on the biochar surface served as weak Brønsted acid sites (Song et al. 2024). The O–H bonds in these groups broke and donated H^+, driving the dehydration of amides to form nitriles. Additionally, hexadecanamide underwent hydrolysis to yield palmitic acid. However, due to the absence of strong acid sites on biochar, the dehydration pathway remained dominant. Subsequently, small molecules derived from pre-cracking (acids, aldehydes, ketones, short-chain alkenes, nitriles, etc.) entered the microporous structure of HZSM-5 and underwent deep catalytic conversion at its Brønsted acid sites (Si–OH-Al). For oxygenates such as aldehydes, H^+ from acid sites protonated the carbonyl oxygen (Bondue And Koper 2019), triggering decarbonylation that generated a carbenium ion. These carbenium ion then induced β-scission of C–C bonds (Cnudde et al. 2018), yielding alkenes. The resulting alkenes underwent cyclization to form cyclic alkenes, followed by aromatization via Diels–Alder reactions (He et al. 2023b). For nitrogen-containing compounds, H^+ attacked nitrogen atoms in heterocycles, leading to C–N bond cleavage and ring opening, which produced amide intermediates. These amides were further denitrogenated and converted to hydrocarbons, ultimately undergoing aromatization to aromatic compounds.

3.3 Stability of the HZSM-5@biochar

The stability of HZSM-5@biochar was evaluated through cyclic testing at a pyrolysis temperature of 500 °C and a catalyst-to-feedstock ratio of 20:1, using HZSM-5 catalyst for comparison. The deactivation parameter D was used to assess the degree of deactivation of the catalyst. Figure 11 provides detailed data. The change of bubble

color represents the change of D value, and the bubble size represents the peak area yield size, and the increase of D value means the increase of peak area yield.

During the cycling experiment of HZSM-5@biochar, the D value of BTX decreased with the increase of cycling number, from 7.27 to 0 (Fig. 11a), but the decrease was lower than that of HZSM-5 (from 10.07 to 0, Fig. 11b). Furthermore, both catalysts showed an increase in the D-value of oxygenates and nitrogenates in the products after six cycles, but it is obvious that the increase of HZSM-5@biochar is smaller than that of HZSM-5. In addition, the peak area yields of nitrogenates and oxygenates from HZSM-5 were basically larger than those from HZSM-5@biochar. After six cycles, the peak area yield of nitrogenates from HZSM-5@biochar increased from 3.02×10^{10} g^{-1} to 1.19×10^{12} g^{-1}, and that of oxygenates increased from 1.02×10^{10} g^{-1} to 5.54×10^{11} g^{-1}. Meanwhile, when using HZSM, the peak area yield of nitrogenates rose from 1.01×10^{12} g^{-1} to 3.10×10^{12} g^{-1} and oxygenates increased from 4.54×10^{11} g^{-1} to 2.29×10^{12} g^{-1}. Hence, compared with HZSM-5, HZSM-5@biochar has more excellent catalytic performance and stability, and its deoxygenation and denitrogenation performance on microalgal biomass was better.

Additionally, three characterization methods (TG, Raman, and SEM) were employed to determine the amount and composition of coke generated on the catalysts. The fresh catalysts and spent catalysts after 1 and 6 cycles (namely, Run 1 and Run 6, respectively) were chosen for analysis.

The coke yield was examined by calculating the difference in weight loss rates of the fresh and spent catalyst, and it can be seen from Fig. 12a that the coke yield of HZSM-5 was higher than that of HZSM-5@biochar, indicating that HZSM-5@biochar was less prone to coking and deactivation than HZSM-5. In addition, attempts to analyze the coke composition by GC/MS, following the method of Li et al. (2025), yielded chromatograms identical to the blank, implying that the coke was highly cross-linked/polymerized and insoluble. Regarding the Raman spectra, the obtained curves were fitted to nine Gaussian peaks (Table S4) to further explore the type of coke (Ayiania et al. 2020b), and Fig. S9 illustrates an instance of curve fitting. The spectrograms appeared to have a G band caused by graphitic carbon and a D band caused by disordered carbon or defective graphitic structures (Kumbhar et al. 2021), and it was also associated with large aromatic ring systems (not less than 6 fused rings) in coke (Chen et al. 2021). The ratio of the intensities of these two bands, I_D/I_G, was utilized to study the carbon structure of the catalyst. The region of A1 and A2 in the spectra (Fig. S9) was connected to breathing modes of smaller aromatic ring systems (5 membered ring structures) as well as various vibrations due to the presence of heteroatoms (oxygen and nitrogen functional groups) (Ayiania et al. 2020b). As seen in Fig. 12b, the I_D/I_G, I_{A1} and I_{A2} of HZSM-5@biochar and HZSM-5 increased from Fresh to Run 6. In terms of I_D/I_G, the increase of HZSM-5@biochar (from 1.90 to 1.98) was much smaller than that of HZSM-5 (from 1.54 to 2.34), indicating that HZSM-5@biochar produced few defects, and the number of large aromatic ring systems (not less than 6 fused rings) in coke on HZSM-5@biochar was less than that on HZSM-5. As for I_{A1} and I_{A2}, the increase of HZSM-5@biochar was larger than that of HZSM-5, implying the presence of more small aromatic ring systems (5 membered ring structures) or nitrogen and oxygen functional groups in the coke of HZSM-5@biochar. SEM was used to examine the external morphologies of the catalysts, which are shown in Figs. 12c–h. The surface morphology of HZSM-5 changed considerably after Run 6, and HZSM-5 particles could be observed in the fresh HZSM-5 catalyst, and as the number of cycles rose, a significant quantity of amorphous substance was found coating the HZSM-5 particle surfaces (Fig. 12d) (He et al. 2023a), making the HZSM-5 particles aggregated (Fig. 12e). The energy dispersive X-ray (EDX) elemental maps showed that the C element content on the surface of HZSM-5 particles gradually increased (yellow circle part), demonstrating that HZSM-5 produced more coke after use. In contrast, the surface morphology and the C content of the HZSM-5 particles in the HZSM-5@biochar catalyst did not change significantly after Run 6 (Fig. 12f–h).

4 Conclusions

Chlorella was first wet torrefied to improve its fuel properties, and then the catalytic pyrolysis was carried out with HZSM-5@biochar. The preliminary deoxygenation and denitrogenation of *Chlorella* were achieved by the wet torrefaction pretreatment. When *Chlorella*-200 was catalyzed by HZSM-5@biochar, the selectivity of aromatics in the pyrolysis products reached 96.06%, including BTX selectivity of 83.24%, with a yield of 94.64 mg g^{-1}. The content of oxygenates and nitrogenates decreased from 82.14% to 3.26%. The catalytic conversion experiments of the model compounds showed that the substances produced by *Chlorella* pyrolysis underwent transformation into aromatics via a variety of reactions, including Diels–Alder reaction, decarboxylation, and decarbonylation. XPS analysis demonstrated that functional groups in the HZSM-5@biochar interacted with pyrolysis vapors and thus changed the catalyst surface carbon structure. In situ DRIFTS further verified that the biochar component in HZSM-5@biochar improved the deoxygenation and denitrogenation effect of the catalyst

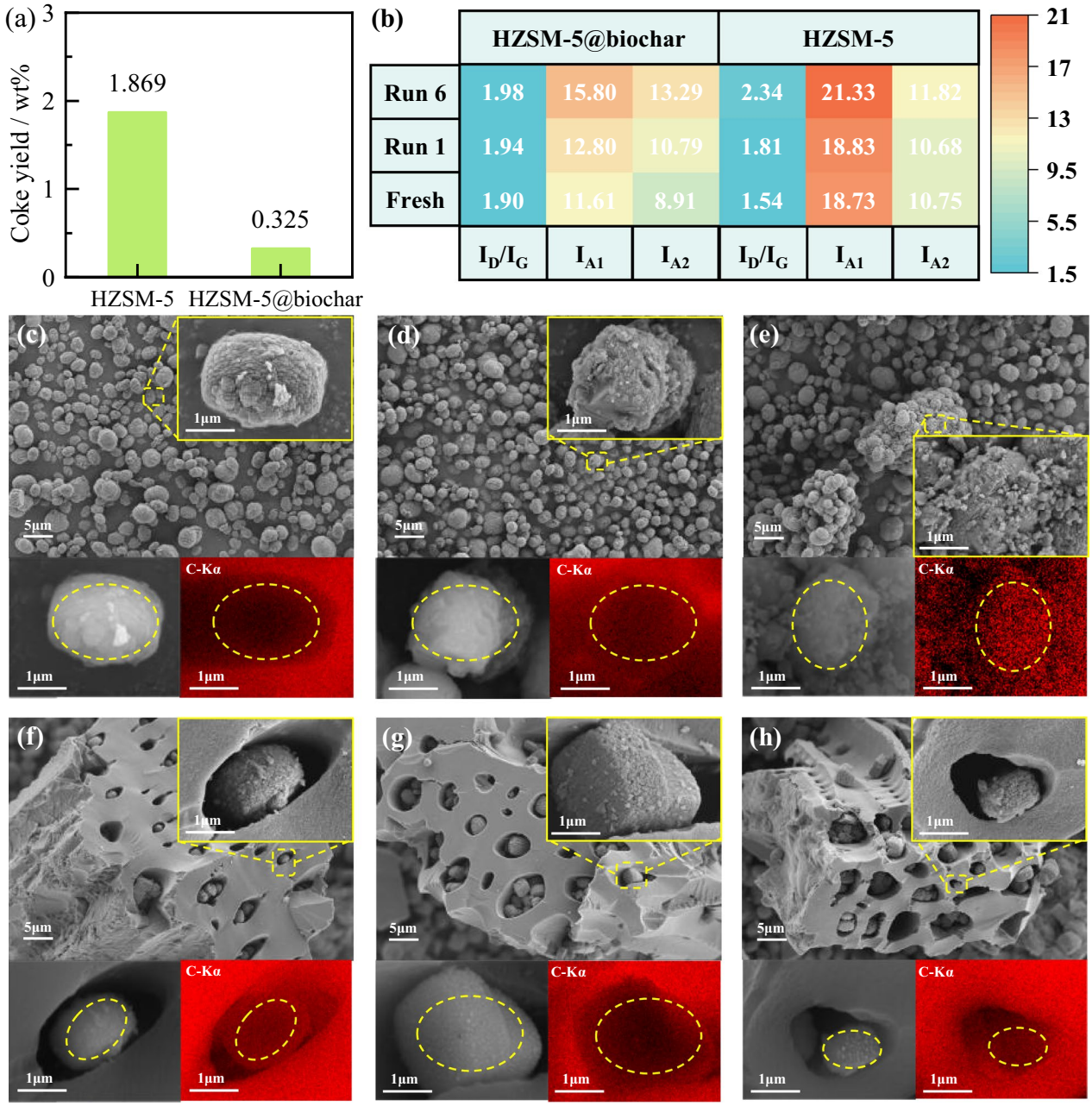

Fig. 12 **a** Comparative analysis of coke yield between HZSM-5 and HZSM-5@biochar. **b** Raman studies of catalysts. SEM images and EDX images of **c** HZSM-5 (Fresh), **d** HZSM-5 (Run 1), **e** HZSM-5 (Run 6), **f** HZSM-5@biochar (Fresh), **g** HZSM-5@biochar (Run 1) and **h** HZSM-5@biochar (Run 6)

mainly in two ways: (1) Pyrolysis molecules tended to enter the weakly acidic biochar first and break relatively unstable chemical bonds such as C=O; (2) Due to the pre-cracking effect of the biochar on the heavy compounds, the possibility of HZSM-5 blockage deactivation was decreased, allowing the reaction to continue up to the step of producing aromatics. In addition, the cycling experiments showed that the HZSM-5@biochar had superior stability to HZSM-5. Coke characterization (TG, Raman and SEM) illustrated that, compared to HZSM-5, HZSM-5@biochar exhibited lower coke yield and coke aromaticity degree, and its surface structure was not significantly altered after cycling experiments.

Supplementary Information

The online version contains supplementary material available at https://doi.org/10.1007/s42773-026-00612-0.

Additional file 1.

Author contributions

Jinye Hu: Conceptualization, Methodology, Investigation, Writing—Original draft, Writing—Review & Editing. Yunpu Wang: Methodology, Writing—Review & Editing. Haiwei Jiang: Methodology, Writing—Review & Editing. Jiabo Wu: Methodology, Investigation. Ting Luo: Methodology, Investigation. Qi Wang: Methodology, Investigation. Yuhang Hu: Methodology, Investigation. Kaisong Hu: Methodology, Investigation. Wenguang Zhou: Methodology, Investigation, Funding acquisition. Liangliang Fan: Conceptualization, Methodology, Investigation, Writing—Original Draft, Writing—Review & Editing, Visualization, Project administration, Funding acquisition. All authors read and approved the final manuscript.

Funding

This work was supported by National Natural Science Foundation of China (Nos. 52566015 and 52360007), Young Talents (academic) of the Ganpo Juncai Support Program of Jiangxi Province, China (20243BCE51078), and Natural Science Foundation of Jiangxi Province, China (No. 20242BAB20105).

Data availability

The datasets used or analyzed during the current study are available from the corresponding author upon reasonable request.

Declarations

Competing interests

The authors declare that they have no known competing financial interests or personal relationships that could have appeared to influence the work reported in this paper.

Author details

[1]School of Resources and Environment, and Key Laboratory of Poyang Lake Environment and Resource Utilization, Ministry of Education, Nanchang University, Nanchang 330031, China. [2]Engineering Research Center for Biomass Conversion, Ministry of Education, Nanchang University, Nanchang 330047, China. [3]Institute of Energy Research, Jiangxi Academy of Sciences, Nanchang 330096, China.

Received: 3 December 2025 Revised: 14 February 2026 Accepted: 26 March 2026
Published online: 17 April 2026

References

Abbas-Abadi MS, Ureel Y, Eschenbacher A et al (2023) Challenges and opportunities of light olefin production via thermal and catalytic pyrolysis of end-of-life polyolefins: towards full recyclability. Prog Energy Combust Sci 96:101046. https://doi.org/10.1016/j.pecs.2022.101046

Anand V, Gautam R, Vinu R (2017) Non-catalytic and catalytic fast pyrolysis of microalga. Fuel 205:1–10. https://doi.org/10.1016/j.fuel.2017.05.049

Ayiania M, Smith M, Hensley AJR et al (2020a) Deconvoluting the XPS spectra for nitrogen-doped chars: an analysis from first principles. Carbon 162:528–544. https://doi.org/10.1016/j.carbon.2020.02.065

Ayiania M, Weiss-Hortala E, Smith M et al (2020b) Microstructural analysis of nitrogen-doped char by Raman spectroscopy: Raman shift analysis from first principles. Carbon 167:559–574. https://doi.org/10.1016/j.carbon.2020.05.055

Bach QV, Chen WH (2017) A comprehensive study on pyrolysis kinetics of microalgal biomass. Energy Convers Manag 131:109–116. https://doi.org/10.1016/j.enconman.2016.10.077

Bach QV, Skreiberg O (2016) Upgrading biomass fuels via wet torrefaction: a review and comparison with dry torrefaction. Renew Sust Energ Rev 54:665–677. https://doi.org/10.1016/j.rser.2015.10.014

Bondue CJ, Koper MTM (2019) A mechanistic investigation on the electrocatalytic reduction of aliphatic ketones at platinum. J Catal 369:302–311. https://doi.org/10.1016/j.jcat.2018.11.019

Chen YJ, Syed-Hassan SSA, Xiong Z et al (2021) Temporal and spatial evolution of biochar chemical structure during biomass pellet pyrolysis from the insights of micro-Raman spectroscopy. Fuel Process Technol 218:106839. https://doi.org/10.1016/j.fuproc.2021.106839

Cheng K, Zhou W, Kang J et al (2017) Bifunctional catalysts for one-step conversion of syngas into aromatics with excellent selectivity and stability. Chem-Us 3(2):334–347. https://doi.org/10.1016/j.chempr.2017.05.007

Chhabra V, Bambery K, Bhattacharya S et al (2020) Thermal and in situ infrared analysis to characterise the slow pyrolysis of mixed municipal solid waste (MSW) and its components. Renew Energy 148:388–401. https://doi.org/10.1016/j.renene.2019.10.045

Cnudde P, De Wispelaere K, Vanduyfhuys L et al (2018) How chain length and branching influence the alkene cracking reactivity on H-ZSM-5. ACS Catal 8(10):9579–9595. https://doi.org/10.1021/acscatal.8b01779

Costil R, Lefebvre Q, Clayden J (2017) Medium-sized-ring analogues of dibenzodiazepines by a conformationally induced smiles ring expansion. Angew Chem Int Ed 56(46):14602–14606. https://doi.org/10.1002/anie.201708991

Dai LL, Wang YP, Liu YH et al (2019) Integrated process of lignocellulosic biomass torrefaction and pyrolysis for upgrading bio-oil production: a state-of-the-art review. Renew Sustain Energy Rev 107:20–36. https://doi.org/10.1016/j.rser.2019.02.015

Dong S, Shen X, Guo Q et al (2023) Valorization of soybean plant wastes in preparation of N-doped biochar for catalytic ozonation of organic contaminants: Atrazine degradation performance and mechanistic considerations. Chem Eng J 472:145153. https://doi.org/10.1016/j.cej.2023.145153

Dong W, Xing J, Chen Q et al (2024) Hydrogen bonds between the oxygen-containing functional groups of biochar and organic contaminants significantly enhance sorption affinity. Chem Eng J 499:156654. https://doi.org/10.1016/j.cej.2024.156654

Du JL, Hu JH, Yang SL et al (2024) A comprehensive investigation of thermal coke formation during rapid non-catalytic pyrolysis of rubber seed oil. Renew Energy 232:121034. https://doi.org/10.1016/j.renene.2024.121034

Eibner S, Margeriat A, Broust F et al (2017) Catalytic deoxygenation of model compounds from flash pyrolysis of lignocellulosic biomass over activated charcoal-based catalysts. Appl Catal B-Environ 219:517–525. https://doi.org/10.1016/j.apcatb.2017.07.071

Fan LL, Ruan R, Li J et al (2020) Aromatics production from fast co-pyrolysis of lignin and waste cooking oil catalyzed by HZSM-5 zeolite. Appl Energy 263:114629. https://doi.org/10.1016/j.apenergy.2020.114629

Figueiredo MC, Ledezma-Yanez I, Koper MTM (2016) In situ spectroscopic study of CO electroreduction at copper electrodes in acetonitrile. Acs Catal 6(4):2382–2392. https://doi.org/10.1021/acscatal.5b02543

Gan YY, Ong HC, Show PL et al (2018) Torrefaction of microalgal biochar as potential coal fuel and application as bio-adsorbent. Energy Convers Manage 165:152–162. https://doi.org/10.1016/j.enconman.2018.03.046

Gu B, Cao JP, Wei F et al (2019) Nitrogen migration mechanism and formation of aromatics during catalytic fast pyrolysis of sewage sludge over metal-loaded HZSM-5. Fuel 244:151–158. https://doi.org/10.1016/j.fuel.2019.02.005

Guo S, Wang Y, Yang L et al (2024) ReaxFF-based molecular dynamics simulation of the impact of potassium on the formation of NH_3 during protein pyrolysis. Energy 313:134059. https://doi.org/10.1016/j.energy.2024.134059

Guo JL, Foo JLC, Ge LY et al (2025) Steam-assisted one-step fabrication of Ni-Ce biochar catalysts for enhanced biomass pyrolysis-steam reforming. Chem Eng J 509:161302. https://doi.org/10.1016/j.cej.2025.161302

He PP, Chen B, Huang L et al (2022) Heterogeneous manganese-oxide-catalyzed successive cleavage and functionalization of alcohols to access amides and nitriles. Chem-Us 8(7):1906–1927. https://doi.org/10.1016/j.chempr.2022.02.021

He M, Ali MF, Song YQ et al (2023a) Study on the deactivation mechanism of HZSM-5 in the process of catalytic cracking of n-hexane. Chem Eng J 451:138793. https://doi.org/10.1016/j.cej.2022.138793

He Y, Chen J, Mo Z et al (2023b) Controlling Diels-Alder reactions in catalytic pyrolysis of sawdust and polypropylene by coupling CO_2 atmosphere and Fe-modified zeolite for enhanced light aromatics production. J Hazard Mater 455:131547. https://doi.org/10.1016/j.jhazmat.2023.131547
Hou C, Zhou CX, Li N et al (2024) Interaction effects between the main components of protein-rich biomass during microwave-assisted pyrolysis. Environ Sci Technol 58(18):7826–7837. https://doi.org/10.1021/acs.est.3c10594
Hu CS, Zhang HY, Wu SL et al (2020) Molecular shape selectivity of HZSM-5 in catalytic conversion of biomass pyrolysis vapors: the effective pore size. Energy Convers Manag 210:112678. https://doi.org/10.1016/j.enconman.2020.112678
Hu JY, Zhou WG, Wang YP et al (2024) Synthesis of HZSM-5@activated carbon for improving aromatic production from catalytic pyrolysis of biomass. Chem Eng J 494:153031. https://doi.org/10.1016/j.cej.2024.153031
Ke L, Wang X, Peng Y et al (2025) Continuous microwave co-pyrolysis of LDPE and PET coupled ex-situ catalysis to monocyclic aromatic hydrocarbons using different structural forms of HZSM-5 as catalysts. Chem Eng J 514:163356. https://doi.org/10.1016/j.cej.2025.163356
Kostyniuk A, Likozar B (2024) Wet torrefaction of biomass waste into value-added liquid product (5-HMF) and high quality solid fuel (hydrochar) in a nitrogen atmosphere. Renew Energy 226:120450. https://doi.org/10.1016/j.renene.2024.120450
Kumar A, Yan BB, Tao JY et al (2022) Co-pyrolysis of de-oiled microalgal biomass residue and waste tires: deeper insights from thermal kinetics, behaviors, drivers, bio-oils, bio-chars, and in-situ evolved gases analyses. Chem Eng J 446:137160. https://doi.org/10.1016/j.cej.2022.137160
Kumbhar D, Palliyarayil A, Reghu D et al (2021) Rapid discrimination of porous bio-carbon derived from nitrogen rich biomass using Raman spectroscopy and artificial intelligence methods. Carbon 178:792–802. https://doi.org/10.1016/j.carbon.2021.03.064
Leng LJ, Yang LH, Chen JF et al (2020) A review on pyrolysis of protein-rich biomass: Nitrogen transformation. Bioresource Technol 315:123801. https://doi.org/10.1016/j.biortech.2020.123801
Li Y, Zhang CS, Liu YG et al (2017) Coke formation on the surface of Ni/HZSM-5 and Ni-Cu/HZSM-5 catalysts during bio-oil hydrodeoxygenation. Fuel 189:23–31. https://doi.org/10.1016/j.fuel.2016.10.047
Li B, Huang HM, Xie X et al (2023) Volatile-char interactions during biomass pyrolysis: effects of AAEMs removal and KOH addition in char. Renew Energy 219:119459. https://doi.org/10.1016/j.renene.2023.119459
Li J, Yang B, Li N et al (2025) Investigation on deactivation periods of ZSM-5/SAPO-34 catalyst in MTA reaction: carbon deposition behavior. Fuel. https://doi.org/10.1016/j.fuel.2025.135207
Liu X, Fan Y, Zhai Y et al (2022) Co-hydrothermal carbonization of rape straw and microalgae: pH-enhanced carbonization process to obtain clean hydrochar. Energy 257:124733. https://doi.org/10.1016/j.energy.2022.124733
Liu L, Fan L, Jin K et al (2023) One-pot synthesis of lignin biochar supported Ni for catalytic pyrolysis of *Chlorella vulgaris* and its model compounds: the formation mechanism of aromatic hydrocarbons. Fuel 341:127558. https://doi.org/10.1016/j.fuel.2023.127558
Liu HY, Zhang J, Shan R et al (2024a) Mechanistic insights into Ga-modified hollow ZSM-5 catalyzed fast pyrolysis of cassava residue. Energy 295:131068. https://doi.org/10.1016/j.energy.2024.131068
Liu Y, Gao LL, Chang GZ et al (2024b) Enhancing reductive conversion of levulinic acid and levulinates to γ-valerolactone: role of oxygen vacancy in MnOx catalysts. Bioresource Technol. https://doi.org/10.1016/j.biortech.2024.131001
Milanese M, Colangelo G, Mellone A et al (2024) Low-energy thermo-chemical conversion processes of municipal wet waste. Therm Sci Eng Prog 54:102852. https://doi.org/10.1016/j.tsep.2024.102852
Nikkhah H, Tavasoli A, Jafarian S (2020) Investigating the influence of acid washing pretreatment and Zn/activated biochar catalyst on thermal conversion of to value-added bio-products. Energy Convers Manag 225:113392. https://doi.org/10.1016/j.enconman.2020.113392
Niu Q, Ghysels S, Wu NN et al (2022) Effects of demineralization on the composition of microalgae pyrolysis volatiles in py-GC-MS. Energy Convers Manag 251:114979. https://doi.org/10.1016/j.enconman.2021.114979
Orrego-Restrepo E, Ordonez-Loza J, Chejne F (2022) Novel methodology for evaluation of cellulose pyrolysis kinetics implementing infrared spectroscopy. J Anal Appl Pyrol 166:105589. https://doi.org/10.1016/j.jaap.2022.105589
Oseke GG, Atta AY, Mukhtar B et al (2021) Increasing the catalytic stability of microporous Zn/ZSM-5 with copper for enhanced propane aromatization. J King Saud Univ Eng Sci 33(8):531–538. https://doi.org/10.1016/j.jksues.2020.07.014
Pham TN, Sooknoi T, Crossley SP et al (2013) Ketonization of carboxylic acids: mechanisms, catalysts, and implications for biomass conversion. ACS Catal 3(11):2456–2473. https://doi.org/10.1021/cs400501h
Shi JJ, Guan JY, Guo DW et al (2016) Nitrogen chemistry and coke transformation of FCC coked catalyst during the regeneration process. Sci Rep 6:27309. https://doi.org/10.1038/srep27309
Song Q, Wang Q, Lu F et al (2024) Influence of Brönsted acid sites on activated carbon-based catalyst for acetylene dimerization. ACS Appl Mater Interfaces 16(6):7345–7352. https://doi.org/10.1021/acsami.3c18423
Su Z, Jin K, Wu J et al (2022) Phosphorus doped biochar as a deoxygenation and denitrogenation catalyst for ex-situ upgrading of vapors from microwave-assisted co-pyrolysis of microalgae and waste cooking oil. J Anal Appl Pyrol. https://doi.org/10.1016/j.jaap.2022.105538
Suarez Ruiz CA, Cabau-Peinado O, van den Berg C et al (2022) Efficient fractionation of lipids in a multiproduct microalgal biorefinery by polymers and ionic liquid-based aqueous two-phase systems. ACS Sustain Chem Eng 10(2):789–799. https://doi.org/10.1021/acssuschemeng.1c06017
Tang ZY, Chen W, Chen YQ et al (2021) Preparation of low-nitrogen and high-quality bio-oil from microalgae catalytic pyrolysis with zeolites and activated carbon. J Anal Appl Pyrol 159:105182. https://doi.org/10.1016/j.jaap.2021.105182
Tian H, Chen L, Huang ZJ et al (2022) Increasing the bio-aromatics yield in the biomass pyrolysis oils by the integration of torrefaction deoxygenation pretreatment and catalytic fast pyrolysis with a dual catalyst system. Renew Energy 187:561–571. https://doi.org/10.1016/j.renene.2022.01.096
Vogt ETC, Fu DL, Weckhuysen BM (2023) Carbon deposit analysis in catalyst deactivation, regeneration, and rejuvenation. Angew Chem Int Ed 62(29):e202300319. https://doi.org/10.1002/anie.202300319
Wang AG, Austin D, Karmakar A et al (2017a) Methane upgrading of acetic acid as a model compound for a biomass-derived liquid over a modified zeolite catalyst. Acs Catal 7(5):3681–3692. https://doi.org/10.1021/acscatal.7b00296
Wang X, Tang X, Yang X (2017b) Pyrolysis mechanism of microalgae *Nannochloropsis* sp. based on model compounds and their interaction. Energy Conv Manag 140:203–210. https://doi.org/10.1016/j.enconman.2017.02.058
Wang YN, Ma WH, Wang DY et al (2017c) Study on the reaction mechanism of the propylene oxide rearrangement via in situ DRIFTS. Chem Eng J 307:1047–1054. https://doi.org/10.1016/j.cej.2016.09.035
Wang YP, Wu QH, Dai LL et al (2018) Co-pyrolysis of wet torrefied bamboo sawdust and soapstock. J Anal Appl Pyrol 132:211–216. https://doi.org/10.1016/j.jaap.2018.02.012
Wang S, Shang H, Abomohra AEF et al (2019) One-step conversion of microalgae to alcohols and esters through co-pyrolysis with biodiesel-derived glycerol. Energy Convers Manage 198:111792. https://doi.org/10.1016/j.enconman.2019.111792
Wang YP, Ke LY, Peng YJ et al (2020) Ex-situ catalytic fast pyrolysis of soapstock for aromatic oil over microwave-driven HZSM-5@SiC ceramic foam. Chem Eng J 402:126239. https://doi.org/10.1016/j.cej.2020.126239
Wu JB, Zhou WG, Wang YP et al (2025) Preparation of hierarchical HZSM-5 loaded Ni for high-grade bio-oil and low coke formation from catalytic co-pyrolysis of microalgae and LDPE. Chem Eng J 526:171240. https://doi.org/10.1016/j.cej.2025.171240
Yu ZY, Guo W, Yang PX et al (2023) In-situ infrared and kinetic characteristics analysis on pyrolysis of tar-rich coal and macerals. Fuel 348:128601. https://doi.org/10.1016/j.fuel.2023.128601
Zhang LQ, Liu JJ, Li DW et al (2022) Research on the thermochemical conversion utilization of nitrogen-rich microalgae: two-step catalytic pyrolysis of *Nannochloropsis sp* over ZSM-5. Energy Convers Manag 258:115475. https://doi.org/10.1016/j.enconman.2022.115475
Zhang J, Wang Z, Cai Y et al (2025) Ultralow-loading subnano [Ptn–Gam]δ+ clusters with Lewis and Brønsted acid functionalities for active Diels-Alder cycloaddition between biomass-derived furans and normal-pressure alkenes. ACS Sustain Chem Eng 13(21):8173–8183. https://doi.org/10.1021/acssuschemeng.5c02727

Zheng YW, Wang Z, Liu C et al (2020) Integrated production of aromatic amines, aromatic hydrocarbon and N-heterocyclic bio-char from catalytic pyrolysis of biomass impregnated with ammonia sources over Zn/HZSM-5 catalyst. J Energy Inst 93(1):210–223. https://doi.org/10.1016/j.joei.2019.03.007

Ziyue T, Chen W, Chen X et al (2023) Thermal behavior and kinetic mechanism of microalgae and model compounds. Fuel 344:128037. https://doi.org/10.1016/j.fuel.2023.128037

Zuo Y, Ye L, Yang W et al (2025) Optimizing ethylene production through enhanced monomolecular β-scission in confined catalytic cracking of olefin. ACS Catal 15(3):1576–1585. https://doi.org/10.1021/acscatal.4c05323